AGU PUBLICATIONS

Geochemistry, Geophysics, Geosystems

RESEARCH ARTICLE
10.1002/2015GC006057

Key Points:
- Mg isotopes of partially dolomitized middle Cambrian limestones are measured
- Mg isotopic systematics of dolomitization is simulated by the convective flow and the DAR model
- Mg isotopes can provide additional constraints on dolomite formation

Correspondence to:
B. Shen,
bingshen@pku.edu.cn

Citation:
Peng, Y., B. Shen, X.-G. Lang, K.-J. Huang, J.-T. Chen, Z. Yan, W.-. Tang, S. Ke, H.-R. Ma, and F.-B. Li (2016), Constraining dolomitization by Mg isotopes: A case study from partially dolomitized limestones of the middle Cambrian Xuzhuang Formation, North China, *Geochem. Geophys. Geosyst.*, *17*, 1109–1129, doi:10.1002/2015GC006057.

Received 11 AUG 2015
Accepted 18 FEB 2016
Accepted article online 26 FEB 2016
Published online 23 MAR 2016

Constraining dolomitization by Mg isotopes: A case study from partially dolomitized limestones of the middle Cambrian Xuzhuang Formation, North China

Yang Peng[1], Bing Shen[1], Xian-Guo Lang[1], Kang-Jun Huang[1], Ji-Tao Chen[2], Zhen Yan[1], Wen-bo Tang[3], Shan Ke[4], Hao-Ran Ma[1], and Fang-Bing Li[1]

[1]Key Laboratory of Orogenic Belts and Crustal Evolution, MOE; School of Earth and Space Sciences, Peking University, Beijing, China, [2]Key Laboratory of Economic Stratigraphy and Palaeogeography, Nanjing Institute of Geology and Palaeontology, Chinese Academy of Sciences, Nanjing, China, [3]School of Mathematical and Statistical Sciences, Arizona State University, Tempe, Arizona, USA, [4]State Key Laboratory of Geological Processes and Mineral Resources, China University of Geosciences, Beijing, China

Abstract The "dolomite problem" refers to the rare dolomite formation in modern oceans that is in sharp contrast to the widespread ancient dolostone in rock record, as well as failure of laboratory inorganic dolomite precipitation at near Earth-surface temperature. Novel Mg isotope systematics provides a promising tool in resolving the "dolomite problem". Here, we develop a protocol to place constraints on the dolomitization process by using Mg isotopes. In this study, we measured Mg isotopic compositions (δ^{26}Mg) of two batches of partially dolomitized limestone samples from the middle Cambrian Xuzhuang Formation in North China. δ^{26}Mg varies between $-0.55‰$ and $-3.18‰$, and shows a negative linear correlation with $\frac{1}{[Mg]}$, suggesting that δ^{26}Mg can be described by a binary mixing between the calcite and dolomite components. Mg isotopic composition of the dolomite component ($\delta^{26}Mg_{dol}$) for the lower sample set that is collected from a 4 m stratigraphic interval containing three high-frequency ribbon rock-packstone cycles is $-1.6‰$, while $\delta^{26}Mg_{dol}$ for the upper sample set (from a thick sequence of ribbon rock) is significantly higher ($-0.3‰$). However, neither mineralogical and elemental compositions, carbon and oxygen isotopes, nor crystal morphologies of dolomite provides diagnostic criteria to differentiate these two batches of samples. $\delta^{26}Mg_{dol}$ of the Xuzhuang limestone is simulated by the Advective Flow (AF) and the Diffusion-Advection-Reaction (DAR) models. The AF model assumes that Mg is transported by advective fluid flows, while the DAR model simulates a contemporaneous seawater dolomitization process, in which Mg is delivered by diffusion. The AF modeling result indicates that δ^{26}Mg of the dolomitization fluid is $+0.4‰$ and $+1.7‰$ for the lower and upper sample sets, respectively. These values are significantly higher than modern and Cenozoic seawater Mg isotopic composition, suggesting that the dolomitization fluid is not contemporaneous seawater. The AF model also predicts spatially heterogeneous $\delta^{26}Mg_{dol}$ with progressive enrichment in ^{26}Mg along the fluid flow pathway. In the DAR model, both dolomite content and $\delta^{26}Mg_{dol}$ of the lower sample set can be simulated by using seawater Mg isotopic composition of $-0.75‰$, thus contemporaneous seawater dolomitization may explain $\delta^{26}Mg_{dol}$ of the Xuzhuang limestone. Furthermore, the DAR model demonstrates spatially homogeneous $\delta^{26}Mg_{dol}$. To differentiate the AF and DAR models, samples from multiple sections are required. Nevertheless, this study implies that Mg isotope might be a useful tool in the study of dolomitization.

1. Introduction

Modern dolomite formation is restricted in a few specific localities, and is characterized by the precipitation of patchily distributed, thin layers of poorly ordered dolomite, in contrast, ancient dolostones in rock record can have platform-wide distribution with thickness up to thousands of meters [*Machel and Mountjoy*, 1986; *Machel*, 2004; *Warren*, 2000]. Scarcity of modern dolomite is echoed by the difficulty of laboratory inorganic precipitation of dolomite at room temperature [*Land*, 1998], suggesting that dolomite formation at low temperature might be kinetically prohibited [*Machel*, 2004; *Warren*, 2000]. It is widely accepted that formation of stoichiometric dolomite in modern environments is kinetically prevented by extensive hydration of seawater Mg^{2+} and the requirement of cation ordering in stoichiometric dolomite [*Goldsmith*, 1953; *Machel*,

2004; *Warren*, 2000]. To precipitate dolomite, the energy barrier imposed by Mg^{2+} hydration must be overcome by increase in Mg/Ca [*Hsü and Siegenthaler*, 1969], fresh water dilution [*Badiozam*, 1973], or microbial mediation [*Roberts et al*., 2013; *Vasconcelos and McKenzie*, 1997; *Vasconcelos et al*., 1995; *Zhang et al*., 2012]. It is also proposed that dolomite formation might be catalyzed by clay minerals [*Wanless*, 1982]. In addition, source of Mg is another key issue that needs to be addressed. There is no doubt that seawater is the primary Mg source for dolomitization [*Land*, 1985], while other Mg sources, such as clay mineral, brine water, and meteoric water, at least locally contribute to dolomite formation [*Badiozam*, 1973; *Kahle*, 1965].

Studies of ancient dolostones traditionally approach with thin section observation, cathodoluminescence, trace element geochemistry, carbon and oxygen isotopes, and strontium isotopes [*Aharon et al*., 1987; *Machel*, 1985; *Machel et al*., 1991; *Mazzullo*, 2000; *Rosen et al*., 1988]. These methodologies provide important constraints on, though not the unique solution to, the origin of ancient dolostones. To further understand the origin of ancient dolostones, we adopt Mg isotopes for the following reasons. First, there are substantial differences in Mg isotopic composition among seawater, sediment porewater, river water, and hydrothermal fluids [*Higgins and Schrag*, 2010; *Ling et al*., 2011; *Mavromatis et al*., 2014; *Pogge von Strandmann et al*., 2008; *Tipper et al*., 2006a, 2006b, 2008], allowing potential implication of Mg isotope to constrain the Mg source of dolomite. Furthermore, dolomite formation is associated with significant fractionation in Mg isotope [*Fantle and Higgins*, 2014; *Higgins and Schrag*, 2010; *Li et al*., 2015], enabling the use of Mg isotope to study the dolomitization process. More importantly, isotopic fractionation for dolomite formation at room temperature has been determined with relatively small uncertainty by a series of detailed studies [*Fantle and Higgins*, 2014; *Higgins and Schrag*, 2010; *Li et al*., 2015; *Mavromatis et al*., 2014; *Rustad et al*., 2010; *Schauble*, 2011].

Thus, the usage of Mg isotope is a promising technique in the study of ancient dolostones [*Fantle and Higgins*, 2014; *Geske et al*., 2015a, 2015b; *Higgins and Schrag*, 2010, 2015; *Huang et al*., 2015; *Mavromatis et al*., 2014]. In previous study, Huang et al discussed the Mg isotope systematics of complete dolomitization, demonstrating that Mg isotopic composition of massive dolostone is determined by many factors [*Huang et al*., 2015]. In addition to massive dolostones, partial dolomitization is more common in carbonate rocks. To constrain the partial dolomitization process by using Mg isotope, here we choose the partially dolomitized limestones of the middle Cambrian Xuzhuang Formation in North China as a case study. Then, we used Mg isotope data with simulations of dolomite formation to constrain the partial dolomitization in limestone.

2. Geological Background

The North China Block preserves a shallow marine carbonate platform deposited during Cambrian and Ordovician time [*Wang*, 1985]. In the Xiaweidian area near Beijing (Figure 1a), the Cambrian succession unconformably overlies the early Neoproterozoic (or Mesoproterozoic) Jineryu Formation [*Gao et al*., 2009], and consists, in ascending order, of the Changping, Manmao, Xuzhuang, Zhangxia, Gushan, and Chaomidian formations. The Changping Formation unconformably overlies the Jineryu Formation, and is composed of medium to thick-bedded dolostone and selectively dolomitized bioturbated lime mudstone/wackstone (the leopard limestone) [*Gao and Qiao*, 2001]. The Changping Formation belongs to the early Cambrian *Megapalaeolenus fengyangensis* trilobite zone [*Zhu and Ma*, 2008]. The contact between the Changping Formation and the overlying purplish red mudstone of the Manmao Formation is not clearly outcropped in the Xiaweidian section, but continuous deposition is inferred from other localities [*Zhu and Ma*, 2008]. Discovery of *Redlichia* (trilobite) implies the early Cambrian of the Manmao Formation, and the presence of halite pseudomorphs suggests the deposition of the Manmao Formation in an arid climatic condition [*Zhu and Ma*, 2008]. The beginning of the middle Cambrian Xuzhuang Formation is marked by the first occurrence of carbonate, representing the beginning of carbonate platform deposition in the North China Block [*Feng et al*., 2002]. The Xuzhuang Formation is conformably overlain by the Zhangxia Formation, which is characterized by the thick-bedded ooids grainstone deposited in shoal complex. Lower part of the overlying Gushan Formation is composed of medium to thick-bedded mudstone, while the upper part consists of ribbon rocks intercalated with intraclastic grainstone/packstone. The upper Cambrian deposition is represented by the ribbon rock intercalated with intraclasts grainstone/packstone of the Chaomidian Formation.

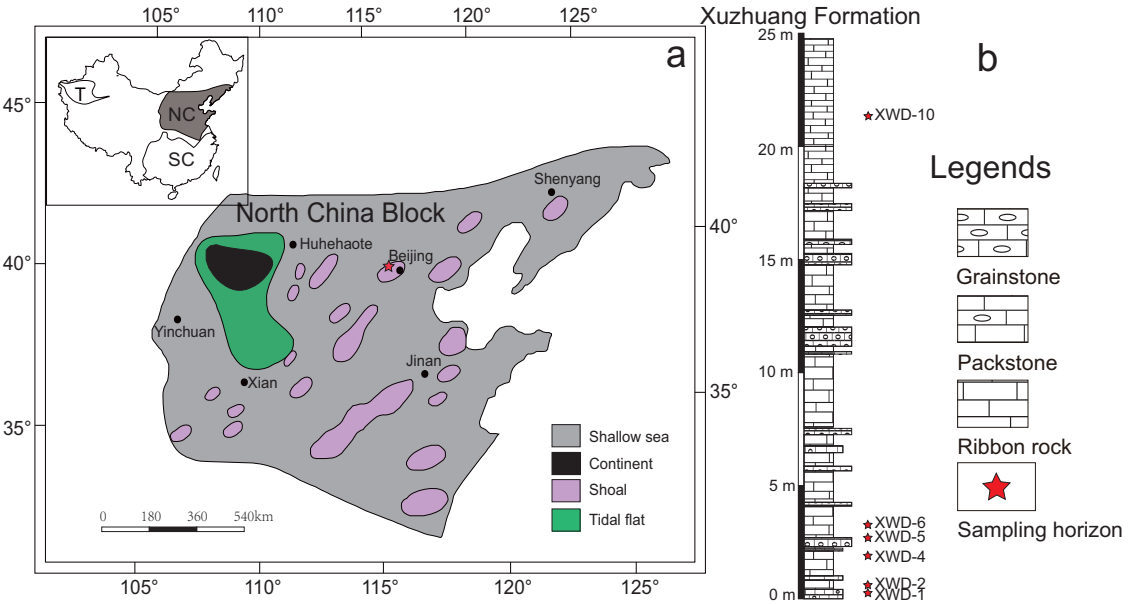

Figure 1. (a) Middle Cambrian paleogeographic map of North China (modified from *Feng et al.* [2002]), showing the sampling locality of the Xiaweidian section (red star) near Beijing. Inset is the current geographic location of North China Block. NC: North China Block; SC: South China Block; T: Tarim Block. (b) Stratigraphic column of the lower Xuzhuang Formation in the Xiaweidian section.

The Xuzhuang Formation is about 80 m thick in the Xiaweidian section, and consists of ribbon rocks intercalated with thin to medium-bedded packstone/grainstone layers (Figures 1b and 2a). Ribbon rock is characterized by alternating limestone and marlstone layers (Figure 2b) [*Chen et al.*, 2010]. Individual cycle of the intercalated packstone/grainstone and ribbon rock has been interpreted as a fifth-order shoaling-upward cycle, reflecting high-frequency low magnitude fluctuation in sea level [*Mei et al.*, 2005; *Osleger and Read*, 1991]. The packstone/grainstone layer has a sharp, erosional contact with the underlying ribbon rock (Figure 2c), suggesting possible erosion during deposition. Furthermore, carbonate grains in the packstone/grainstone layers include ooids, bioclasts, and intraclasts (Figure 2d). These observations imply that the packstone/grainstone layers may represent storm deposits with carbonate grains transported by storm-induced currents from nearby grainy shoal to below the fair-weather wave base, reflecting frequent storm perturbation of subtidal deposition.

Six limestone samples were collected from the lower part of the Xuzhuang Formation. The first five samples were collected from a 4 m interval, containing three high-frequency packstone/grainstone-ribbon rock cycles with individual cycle of less than 2 m thick. In contrast, the last sample was collected from a thick (>7 m thick) ribbon rock layer, ~17 m above the fifth specimen (Figure 1b), representing a low-frequency cycle.

3. Method

3.1. Sample Preparation

Fresh carbonate rocks were split into two parts using a rock saw, and mirrored thin (30 μm) and thick (2 mm) sections were prepared. Petrographic studies were conducted under thin-section observation. Calcite and dolomite were distinguished by stain of Alizarin Red S. After staining, calcite is stained red, while dolomite remains colorless. Under the guidance of thin section observation, sample powders (5–20 mg for each sample) were drilled using a hand-held micromill from the corresponding polished thick section. Considering the compositional heterogeneity in limestone, in order to capture the whole range of compositional and textural variations, multiple powder samples were collected from each thick section (Table 1). Powder samples were used for Mg isotope, C and O isotopes, and elemental analyses.

3.2. Mg Isotope Analysis

Powder samples were dissolved by 4 mL of 0.5*N* acetic acid in a centrifuge tube, and tubes were placed in an ultrasonic bath for 30 min to allow complete dissolution of carbonate component. After centrifugation,

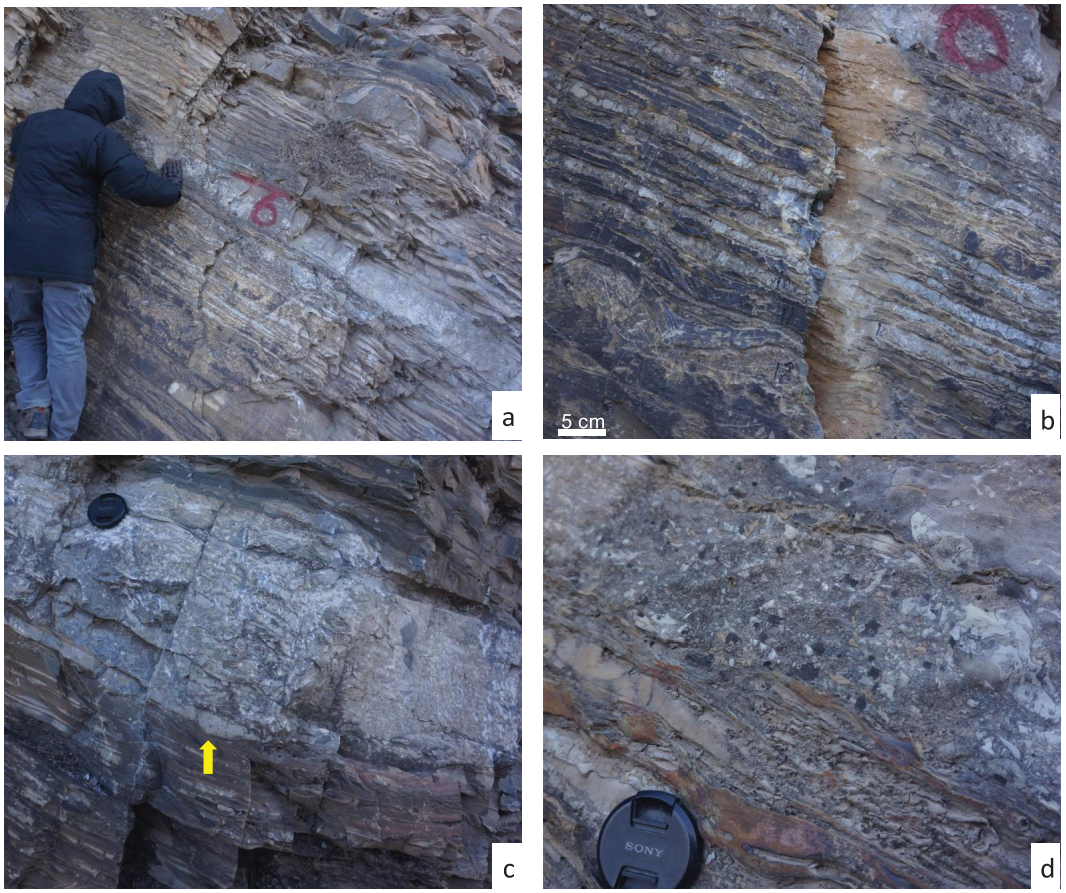

Figure 2. (a) Outcrop photograph of the lower Xuzhuang Formation in the Xiaweidian section, showing ribbon rocks intercalated with grainstone/packstone layers. (b) Ribbon rocks consisting of alternating lime mudstone (white) and marlstone (yellow) layers. (c) Sharp, irregular contact (yellow arrow) between ribbon rock and the overlying grainstone/packstone layer. (d) Close-up view of the grainstone bed showing different carbonate grains.

Table 1. Mg Isotopic Compositions of the Xuzhuang Limestone[a]

Specimen	Sample	Description	Mg/Ca	δ^{26}Mg	2SD	δ^{25}Mg	2SD	n
XWD-1	XWD-1-1	P/G	0.06	−2.58	0.02	−1.33	0.05	3
	XWD-1-2	P/G	0.03	−2.54	0.08	−1.32	0.04	3
	XWD-1-3	P/G	0.02	−3.18	0.04	−1.67	0.03	3
XWD-2	XWD-2-1	RR	0.32	−1.67	0.04	−0.87	0.04	3
	XWD-2-2	RR	0.10	−1.40	0.03	−0.75	0.05	3
XWD-4	XWD-4-1	RR-M	0.15	−1.69	0.03	−0.88	0.01	3
	XWD-4-2	RR-L	0.04	−1.83	0.04	−0.97	0.05	3
	XWD-4-3	RR-L	0.04	−2.22	0.04	−1.17	0.05	3
	XWD-4-4	RR-M	0.37	−1.84	0.01	−0.96	0.05	3
XWD-5	XWD-5-1	P/G	0.02	−3.17	0.02	−1.65	0.04	3
	XWD-5-2	P/G	0.02	−3.08	0.02	−1.61	0.03	3
	XWD-5-3	P/G	0.02	−3.18	0.03	−1.63	0.04	3
XWD-6	XWD-6-1	RR-L	0.04	−2.30	0.08	−1.20	0.05	3
	XWD-6-2	RR-M	0.28	−1.82	0.03	−0.95	0.07	3
	XWD-6-3	RR-L	0.04	−2.14	0.02	−1.12	0.05	3
XWD-10	XWD-10-1	RR-M	0.09	−0.55	0.04	−0.30	0.06	3
	XWD-10-2	RR-L	0.06	−1.20	0.05	−0.60	0.06	3
	XWD-10-3	RR-M	0.11	−0.71	0.06	−0.35	0.09	3
	XWD-10-4	RR-L	0.05	−0.95	0.08	−0.50	0.05	3
GSB Mg		Standard		−2.06	0.04	−1.06	0.03	18
BCR-2		Standard		−0.17	0.06	−0.08	0.05	3

[a]All errors (2SD) are 2 standard deviations of the mean value; n is the number of measurements. G/P: grainstone/packstone; RR: ribbon rock; RR-L: lime mudstone layer in ribbon rock; RR-M: marlstone layer in ribbon rock.

supernatant was prepared for Mg isotope analyses. Magnesium was purified by cation exchange chromatography at Peking University. Detail procedure of Mg purification has been reported in previous studies [*Huang et al*., 2015; *Shen et al*., 2009, 2013]. We provide a brief description as follows. First, sample solution containing ~25–30 μg of Mg was eluted through column #1 (loaded with 1.8 mL of Bio-Rad 200–400 mesh AG50W-X12 resin) to separate Mg from Ca. Mg fraction was collected in 4 mL of 12*N* HCl, whereas Ca was retained in the resin. In the following column #2 (loaded with 0.5 ml of Bio-Rad 200–400 mesh AG50W-X12 resin), Mg was separated from all other matrix. Cr, Al, Fe, Na, and K were sequentially eluted out by 0.8 mL of 1*N* HCl, 3 mL of 1*N* $HNO_3 + 0.5N$ HF, and 1 mL of 1*N* HNO_3. Mg fraction was collected with 5 mL of 2*N* HNO_3. To ensure a clean Mg fraction, each sample passed through column #1 three times, followed by two passes of column #2. After purification, Ca/Mg, Al/Mg, Na/Mg, K/Mg, and Fe/Mg are less than 0.05, and Mg recovery rates are higher than 99%.

Magnesium isotopic ratios were measured by a Thermo Scientific Neptune Plus high-resolution multicollector Inductively Coupled Plasma Mass Spectrometry (MC-ICP-MS) at Isotope Laboratory of China University of Geosciences, Beijing. Measurements were conducted by the standard-sample bracketing method so as to correct for instrumental mass bias and drift. Samples were bracketed by an in-house standard solution (FZT). Sample solutions were diluted to ±10% of the concentration of the standard. All analyses are reported in the delta notation as per mil (‰) deviation relative to the DSM-3 standard [*Galy et al*., 2003]:

$$\delta^{x}\mathrm{Mg} = 1000 \times \left[\frac{\left({}^{x}\mathrm{Mg}/{}^{24}\mathrm{Mg} \right)_{\mathrm{sample}}}{\left({}^{x}\mathrm{Mg}/{}^{24}\mathrm{Mg} \right)_{\mathrm{DSM3}}} - 1 \right] \quad (1)$$

where x is the mass number 25 or 26.

Solution containing 400 ppb Mg was introduced into plasma via a standard H-skimmer cone and an ESI PFA MicroFlow (~50 μL/min) nebulizer with a quartz Scott-type spray chamber. Analyses were performed at low mass resolution mode, simultaneously measuring ^{26}Mg, ^{25}Mg, and ^{24}Mg. A 400 ppb solution typically yields a ^{24}Mg signal of ~6 V; while the procedure blank is typically $< 10^{-4}$ V for ^{24}Mg, significantly lower than the sample signal.

The internal precision of the measured ^{26}Mg/^{24}Mg ratio was determined by repeated runs (three times) of the same sample solution during a single analytical session, and is better than 0.1‰ (2SD). The analytical accuracy was determined by the measurements of a synthetic in-house standard (GSB-Mg) and a USGS standard (BCR-2). Multiple analyses of GSB-Mg yield δ^{26}Mg value of -2.06 ± 0.04‰ (Table 1), which is consistent with the given value of -2.05 ± 0.05‰ (2σ). Results for BCR-2 analyzed during the course of this study (-0.17 ± 0.06‰ (2σ)) are consistent with previously published data [*Opfergelt et al*., 2012; *Pogge von Strandmann et al*., 2011].

3.3. Carbon and Oxygen Isotope Analysis

δ^{13}C and δ^{18}O were measured using a MAT 253 isotope ratio mass spectrometry (IRMS) at Nanjing Institute of Geology and Palaeontology, Chinese Academy of Sciences. About 80–100 μg of carbonate powder was reacted with orthophosphoric acid for 150–200 s at 72°C in a Kiel IV carbonate device. Isotopic ratios are reported as δ-notation with respect to the VPDB standard. The analytical precision is better than 0.05‰ for δ^{13}C and 0.1‰ for δ^{18}O.

3.4. ICP-OES Analysis

Approximately 10 mg of microdrilled carbonate powder was dissolved in 10 mL of 0.5*N* Acetic acid. After complete dissolution in an ultrasonic bath, solution was centrifuged for 10 min at 3000 rpm. Supernatant was collected for the element composition determination. Elemental analyses were conducted at Peking University using a Spectro Blue Sop inductively coupled plasma optical emission spectrometer (ICP-OES) fitted with a Water Cross-flow nebulizer. All analyses were calibrated by a series of gravimetric standards with different concentrations (ranging from 0.1 to 10 ppm) that were run before and after every twenty sample measurements. The external reproducibility for the major and minor elements (Na, Mg, Al, K, Ca, Fe, Mn, Sr) in carbonate samples is ±5%.

3.5. XRD Analysis

About 2g of fresh carbonate chips were crushed to fine powders (<200 mesh). The mineralogical compositions of the powder samples were analyzed using a PANalytical X'Pert Pro MPD X-ray Diffractmeter at Peking University. X-ray was generated by a Cu source with the working voltage of 40 kV and current of 40 mA. Minerals were identified by the peak position, while the mineralogical concentrations were quantitatively determined by measuring the integrated areas under peaks.

4. Petrography of the Xuzhuang Limestone

The Xuzhuang Formation is composed of ribbon rocks intercalated with thin to medium-bedded grainstone/packstone layers. Ribbon rock, also known as the limestone-marl alternations, consists of the alternating limestone and marlstone layers (Figures 2a, 2b, 3a, and 3b) [*Chen*, 2009; *Munnecke and Samtleben*, 1996; *Westphal and Munnecke*, 2003; *Westphal et al*., 2000]. The calcareous components in the ribbon rock are composed of micrite, containing negligible amounts of carbonate grains. Carbonate grains in the grainstone/packstone layers are dominated by ooids and bioclasts with rare occurrences of carbonate intraclasts. The fabric of grainstone/packstone is largely preserved, although the internal structures of some carbonate grains are obliterated by recrystallization or dolomitization (Figure 3c).

The marlstone layers of the ribbon rock contain <40 wt % carbonate (calcite + dolomite) and >20 wt % clays, while the limestone layers contain 40∼75 wt % carbonate and 0∼20 wt % clays (Table 2). The intercalated grainstone/packstone layers are more calcareous (Figure 3c), containing >85 wt % carbonate and no clay (below the detection limit of XRD) (Table 2). In addition to carbonate and clay minerals, all samples contain various amounts of quartz and albite (Table 2). There is a crude correlation between clay mineral content and nonclay detrital (quartz and albite) content (Figure 4a). Clay minerals are identified as chlorite, mica, and illite. Chlorite is present in all samples that contain clay minerals, while mica and illite do not cooccur in the same sample (Table 2). Furthermore, there is a positive correlation between chlorite and total clay mineral content (Figure 4b). The Xuzhuang limestones are partially dolomitized, and all the Xuzhuang samples contain nearly the same amount of dolomite (excluding 1 outlier (12.7%), average dolomite wt % = 4%, ranging from 2.7% to 5.8%). There is no correlation between dolomite wt % and carbonate wt % (Figure 4c) as well as dolomite wt % and clay wt % (Figure 4d).

5. Geochemical Results

δ^{26}Mg of the Xuzhuang limestone samples ranges from −0.55‰ to −3.18‰ (Table 1). The upper sample set (XWD-10) is significantly heavier (ranging from −0.55‰ to −1.20‰) than the lower sample set (varying between −1.40‰ and −3.18‰; Figure 5). Mg/Ca (mol ratio) of the carbonate fraction also shows a wide range of variation, ranging from 0.02 to 0.36 (Table 1). δ^{13}C varies between −1.37‰ and +0.27‰, while δ^{18}O ranges from −12.71‰ to −8.94‰ (Table 3). Sr content of the lower and upper sample sets ranges from 400 to 860 ppm (average = 701 ppm, n = 15) and from 931 to 1035 ppm (average = 1002 ppm, n = 4), respectively, while Mn concentration varies between 925 and 3859 ppm (average = 1634 ppm, n = 15) for the lower sample set and between 2749 and 4570 ppm (average = 3655 ppm, n = 4) for the upper sample set (Table 3).

6. Interpretation and Discussion

6.1. Dolomite in the Xuzhuang Limestone

Regardless of different lithologies and mineralogical compositions, the Xuzhuang limestone samples contain nearly the same quantity of dolomite (Figure 4c). Dolomites in ribbon rocks and in grainstone/packstone layers have distinct crystal shapes. The fabric of grainstone/packstone is generally preserved after dolomitization (Figure 3c). Dolomites in the inter-grain spaces are anhedral (nonplanar) (Figure 3e), while the crystal shape is confined by grain boundaries in dolomitized carbonate grains (Figure 3f). In contrast, dolomites in ribbon rocks are subhedral with planar crystal edges (planar-s) (Figure 3d), and range from 20 to 100 μm in size. In both grainstone/packstone and ribbon rocks, dolomite crystals contain abundant calcite inclusions (Figure 3f), and sometimes show turbid core and limpid rim structure (Figure 3f). These

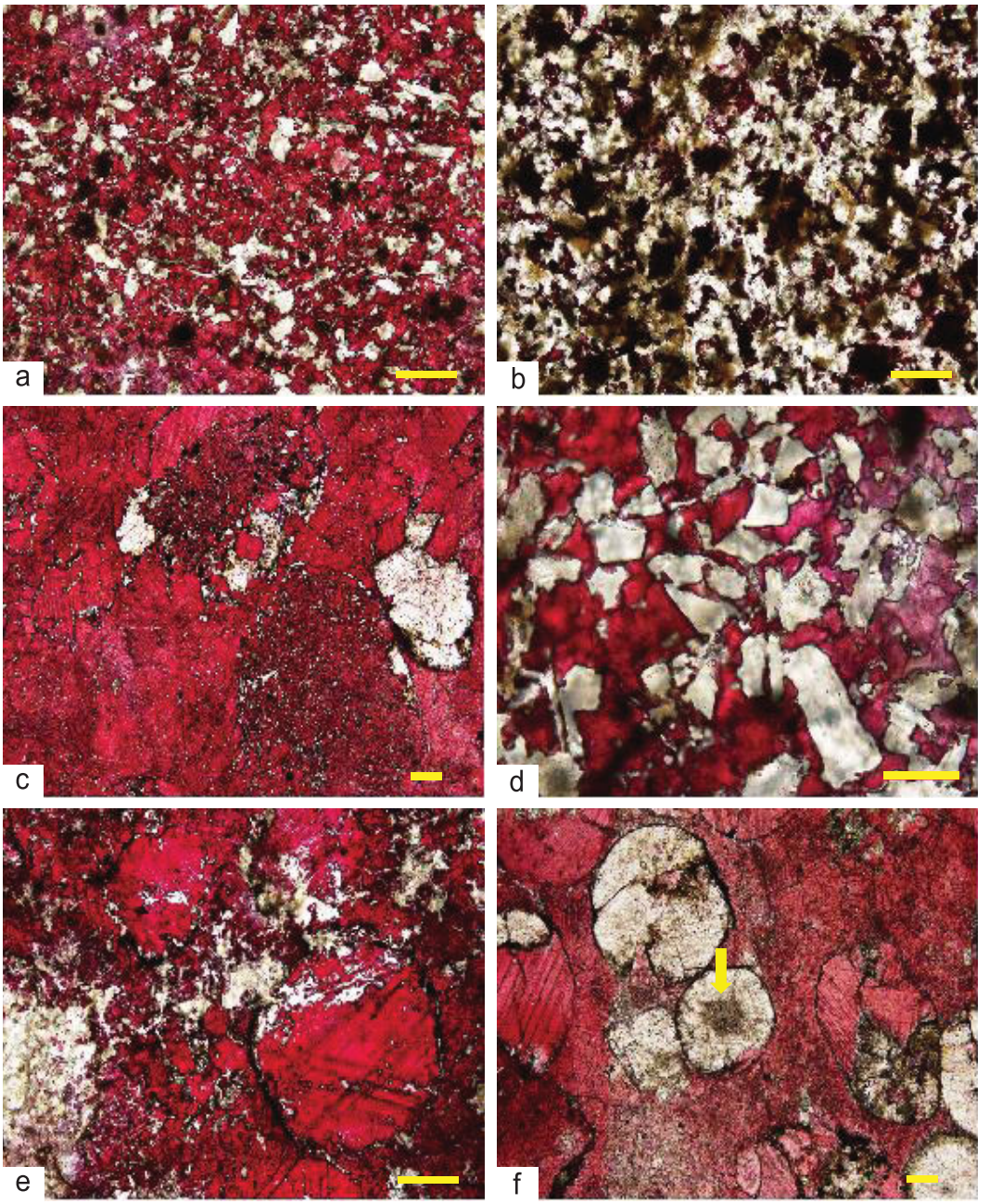

Figure 3. Photomicrographs of the partially dolomitized Xuzhuang limestone. (a) Lime mudstone layer in ribbon rock; (b) Marlstone layer in ribbon rock; (c) Packstone layer, showing partial dolomitization with less dolomite content than ribbon rock (a and b); (d) Subeuhedral dolomite crystals in ribbon rock; (e) Anhedral dolomite crystals in the intergranular spaces of grainstone and partially dolomitized and recrystallized carbonate grains; (f) Dolomitized carbonate grains containing abundant inclusions and showing limpid rim and turbid core structure (yellow arrow), suggesting the replacive origin of dolomite. Calcite is stained red, while dolomite is unstained. Scale bars are 150 μm for Figure 3d and 100 μm for all others.

observations suggest replacive origin of dolomite. Dolomites in the lower and upper sample sets have similar crystal morphology, and thus cannot be simply differentiated by petrographic observations.

We further measured carbon and oxygen isotopes and trace element contents. Carbon and oxygen isotopes are the canonical method in the study of dolomite. The isotopic compositions of dolomite are determined by temperature of precipitation and the isotopic compositions of dolomitization fluid [*Machel*, 2004; *Tucker and Wright*, 1990; *Warren*, 2000]. For example, dolomite derived from bacterial sulfate reduction has

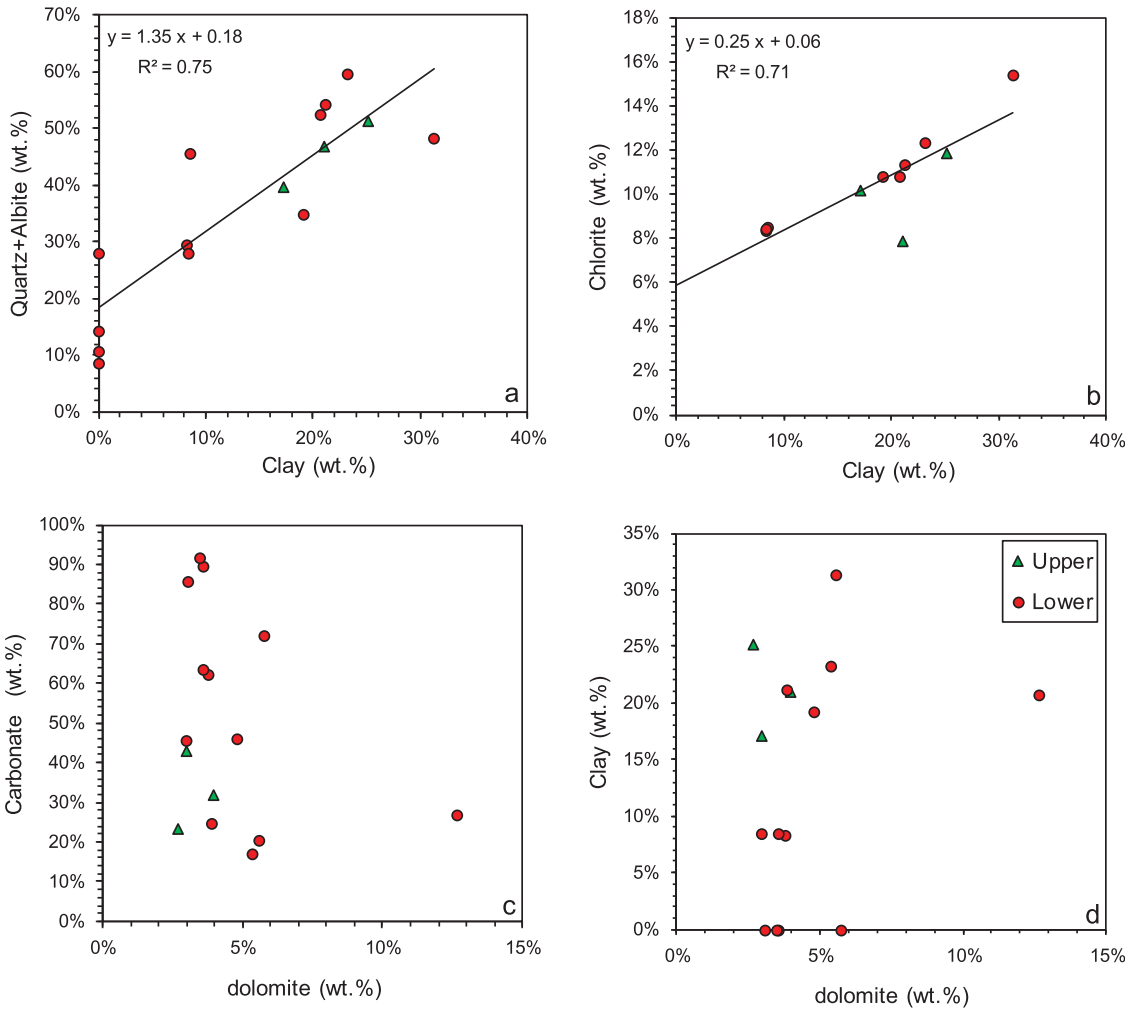

Figure 4. Cross plots of mineralogical compositions of the Xuzhuang limestone. (a) Clay mineral wt. % versus non-clay detrital material (quartz + albite) wt. %. (b) Clay mineral wt. % versus Chlorite wt. %. (c) Carbonate wt. % versus dolomite wt. %. (d) Clay mineral wt. % versus dolomite wt. %.

negative $\delta^{13}C$, while methanogenetic dolomite is characterized by positive $\delta^{13}C$ [*Mazzullo*, 2000]. Normally, different types of dolomite can be differentiated by plotting on a $\delta^{18}O$-$\delta^{13}C$ crossplot [*Warren*, 2000]. The lower sample set of the Xuzhuang limestone has slightly higher $\delta^{13}C$ ($-0.18‰$ versus $-1.25‰$) and $\delta^{18}O$ ($-11.41‰$ versus $-12.55‰$) than the upper sample set (Figure 6a). However, such subtle differences in $\delta^{13}C$ and $\delta^{18}O$ cannot be used as the diagnostic criteria, because different types of dolomite have large degree of overlap in a $\delta^{18}O$-$\delta^{13}C$ crossplot [*Mazzullo*, 2000; *Warren*, 2000].

Furthermore, trace element (Sr, Mn, Na, Fe) can be used to constrain the origin of dolomite as well. Trace element contents in dolomite are determined by the composition of dolomitization fluids, degree of water-rock interaction, distribution coefficient between dolomite and solution, and the mineralogy of parental carbonate rock (aragonite versus high-Mg calcite versus low-Mg calcite) [*Machel*, 2004; *Tucker and Wright*, 1990; *Warren*, 2000], but the interpretation of trace element data is not straightforward, largely due to less constraint on the distribution coefficients [*Warren*, 2000]. In fact, even for the same type of dolomite, trace element contents show a wide range of variation [*Mazzullo*, 2000]. For the Xuzhuang samples, the lower sample set has lower Sr (701 versus 1003 ppm) and Mn (1637 versus 3659 ppm) (Figure 6b), but an overlapping range of Mn/Sr (Figure 6c). Therefore, trace element data provide no definitive constraint on the origin of dolomite in the Xuzhuang limestone.

Based on the aforementioned methodologies, it is still unclear whether the lower and upper sample sets have undergone different dolomitization processes. It is also uncertain whether contemporaneous seawater,

Table 2. Mineralogical Compositions and Mg/Ca Ratios of the Xuzhuang Limestone[a]

Sample No.	Quartz (wt %)	Albite (wt %)	Dolomite (wt %)	Calcite (wt %)	Chlorite (wt %)	Mica (wt %)	Illite (wt %)	Mg/Ca (mol/mol)
XRD-2A	53.5%	6.3%	5.4%	11.6%	12.3%	10.9%	n.d.	0.25
XRD-2B	34.9%	n.d.	4.8%	41.1%	10.8%	8.4%	n.d.	0.05
XRD-4A	47.9%	6.5%	3.9%	20.6%	11.3%	9.9%	n.d.	0.12
XRD-4B	25.2%	20.6%	3.0%	42.7%	8.5%	n.d.	n.d.	0.03
XRD-4C	28.1%	n.d.	5.8%	66.1%	n.d.	n.d.	n.d.	0.04
XRD-4D	52.4%	n.d.	12.7%	14.2%	10.8%	n.d.	9.9%	0.30
XRD-5A	10.6%	n.d.	3.6%	85.8%	n.d.	n.d.	n.d.	0.02
XRD-5B	8.5%	n.d.	3.5%	88.0%	n.d.	n.d.	n.d.	0.02
XRD-5C	14.4%	n.d.	3.1%	82.5%	n.d.	n.d.	n.d.	0.02
XRD-6A	29.4%	n.d.	3.8%	58.4%	8.3%	n.d.	n.d.	0.03
XRD-6B	48.2%	n.d.	5.6%	14.9%	15.4%	n.d.	15.9%	0.22
XRD-6C	28.1%	n.d.	3.6%	59.9%	8.4%	n.d.	n.d.	0.03
XRD-10A	45.3%	6.0%	2.7%	20.7%	11.9%	n.d.	13.3%	0.04
XRD-10B	34.1%	5.7%	3.0%	40.0%	10.2%	n.d.	7.0%	0.03
XRD-10C	39.3%	7.6%	4.0%	28.0%	7.9%	n.d.	13.2%	0.06

[a]Mineralogical compositions are determined by XRD, while Mg/Ca ratios are measured by ICP-OES. n.d.: not detected due to below the detection limit.

modified seawater, or subsurface brines could be the primary Mg source for dolomitization. Nevertheless, the lower and upper sample sets have distinct Mg isotopic compositions (Figures 6d–6f), suggesting that Mg isotopes may provide additional constraints on the dolomitization of the Xuzhuang limestone.

6.2. Mg Isotopic Systematics of the Partially Dolomitized Xuzhuang Limestone

To study the Mg isotopic compositions of partially dolomitized limestone, complete dissolution of the calcareous component (both calcite and dolomite) is required. Incomplete dissolution would result in preferential dissolution of calcite, which has different δ^{26}Mg from that of dolomite [*Huang et al*., 2015]. On the other hand, potential contamination from clay minerals must be avoided as well. Clay minerals contain various amounts of Mg and have distinct δ^{26}Mg compared to carbonate minerals [*Awwiller*, 1993; *Wimpenny et al*., 2014]. Release of Mg from clay minerals would cause a mixing of carbonate-Mg and clay-Mg. In order to completely dissolve the calcareous component and avoid clay mineral dissolution, powder samples were dissolved in 0.5*N* acetic acid, and reactions were allowed in ultrasonic bath for 30 min.

To test the validity of dissolution procedure, we ran an experiment, in which carbonate and shale samples were dissolved by different types of acids. Limestone (GSR-13) and shale (GSR-5) standards were dissolved by 0.5*N* acetic acid, 1*N* acetic acid, 1*N* HCl, 3*N* HCl, and a mixture of concentrated HNO_3 and HF (3:1 volume ratio). A mixture of concentrated HNO_3 and HCl would completely dissolve both calcareous and siliciclastic components. In the shale dissolution (GSR-5), Al content shows an increasing trend from acetic acid, HCl, and HNO_3+HF solutions, and 0.5*N* acetic acid would cause ~1% release of Al from shale (Figure 7a), suggesting negligible dissolution of clays by 0.5*N* acetic acid. For the carbonate dissolution (GSR-13), Ca content remains nearly constant regardless of the types and concentrations of acid (Figure 7b), implying that 0.5*N* acetic acid can dissolved carbonate components completely.

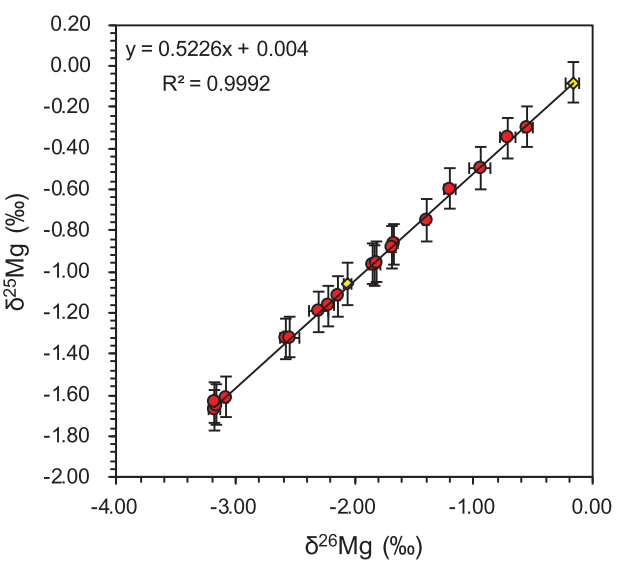

Figure 5. δ^{26}Mg versus δ^{25}Mg cross-plot for the Xuzhuang limestone samples and standards.

The above experiment is further supported by the mineralogical compositions

Table 3. Carbon and Oxygen Isotopes and Elemental Compositions of the Xuzhuang Limestone[a]

Sample	Al (ppm)	Fe (ppm)	Na (ppm)	K (ppm)	Mn (ppm)	Sr (ppm)	Mn/Sr	$\delta^{13}C$ (‰)	$\delta^{18}O$ (‰)
XW-1-1	9041	9173	399	8411	1528	547	2.79	−1.33	−10.10
XW-1-2	2380	5791	212	1888	1594	817	1.95	−0.20	−11.75
XW-1-3	547	4957	94	427	991	557	1.78	0.13	−11.61
XW-2-1	33578	59865	2315	18495	1984	754	2.63	0.04	−11.22
XW-2-2	6406	15126	495	2803	1250	792	1.58	−0.05	−11.84
XW-4-1	21743	27539	2262	9866	1828	589	3.10	−0.34	−11.03
XW-4-2	5153	10283	559	2616	953	860	1.11	0.02	−11.77
XW-4-3	2610	9848	223	1461	961	859	1.12	0.13	−11.93
XW-4-4	20553	46970	1220	13215	2039	629	3.24	0.16	−10.93
XW-5-1	922	6411	182	630	1522	780	1.95	−0.22	−12.22
XW-5-2	865	6053	140	770	1525	537	2.84	−0.32	−11.52
XW-5-3	645	5824	172	537	2482	840	2.95	−0.14	−12.39
XW-6-1	2786	10100	249	1690	952	746	1.28	−0.59	−11.95
XW-6-2	35933	32924	983	24367	3859	400	9.65	0.27	−8.94
XW-6-3	3683	10039	285	2046	1037	800	1.30	−0.33	−11.89
XW-10-1	17094	23761	989	8368	4252	931	4.57	−1.25	−12.52
XW-10-2	8008	16275	484	4472	4570	1035	4.41	−1.09	−12.71
XW-10-3	11638	22305	735	8895	3048	1031	2.96	−1.28	−12.60
XW-10-4	5868	15411	288	3120	2749	1013	2.71	−1.37	−12.38

[a]The elemental data represent the composition of calcareous component of the Xuzhuang limestone.

measured by XRD and elemental data from ICP-OES analyses of the same sample. A significant positive linear correlation ($R^2 = 0.94$) between Mg/Ca (molar ratio) and the molar fraction of dolomite in the carbonate component [dolomite/(dolomite + calcite)] with the slope of the regression line of 1.064 suggest that only calcite and dolomite were dissolved by 0.5*N* acetic acid (Figure 8). The abnormally high Al and Fe content in the solution cannot be attributed to clay dissolution (Table 3). We speculate that high Al and Fe contents might result from dissolution of $Fe(OH)_3$, whose precipitation might be associated with Al colloids.

Thus, $\delta^{26}Mg$ can be modeled by a binary mixing between the calcite and dolomite components. The mass and isotope balances can be described by equations (2) and (3), respectively:

$$[Mg] = (1-F)\times[Mg]_{cal} + F\times[Mg]_{dol} \tag{2}$$

$$\delta^{26}Mg = \frac{(1-F)\times[Mg]_{cal}\times\delta^{26}Mg_{cal} + F\times[Mg]_{dol}\times\delta^{26}Mg_{dol}}{[Mg]} \tag{3}$$

where [Mg] and $\delta^{26}Mg$ are Mg concentration and isotopic composition of bulk sample; $[Mg]_i$ and $\delta^{26}Mg_i$ denote Mg concentration and isotopic composition of component *i*, where the subscripts $_{cal}$ and $_{dol}$ represent the calcite and dolomite components, respectively. F is the mass fraction of the dolomite component in the calcite-dolomite binary mixing system. Combining equations (2) and (3), we arrive at:

$$\delta^{26}Mg = \frac{[Mg]_{dol}[Mg]_{cal}(\delta^{26}Mg_{cal} - \delta^{26}Mg_{dol})}{([Mg]_{dol} - [Mg]_{cal})}\left(\frac{1}{[Mg]}\right) + \frac{[Mg]_{dol}\delta^{26}Mg_{dol} - [Mg]_{cal}\delta^{26}Mg_{cal})}{([Mg]_{dol} - [Mg]_{cal})} \tag{4}$$

Equation (4) defines a linear line with the form of $\delta^{26}Mg = a\times\frac{1}{[Mg]} + b$, where a and b are the slope and intercept, respectively:

$$a = \frac{[Mg]_{dol}[Mg]_{cal}(\delta^{26}Mg_{cal} - \delta^{26}Mg_{dol})}{([Mg]_{dol} - [Mg]_{cal})} \tag{5}$$

$$b = \frac{[Mg]_{dol}\delta^{26}Mg_{dol} - [Mg]_{cal}\delta^{26}Mg_{cal})}{([Mg]_{dol} - [Mg]_{cal})} \tag{6}$$

For the lower sample set (including XWD-1, XWD-2, XWD-4, XWD-5, and XWD-6), $\frac{1}{[Mg]}$ and $\delta^{26}Mg$ show a negative linear correlation (Figure 9a, $R^2 = 0.81$), suggesting that these specimens can be defined by a binary mixing between the calcite and dolomite components with fixed isotopic values, i.e., dolomites in these samples have the same $\delta^{26}Mg$. The negative correlation implies that the dolomite component with lower $\frac{1}{[Mg]}$ is characterized by higher $\delta^{26}Mg_{dol}$, while the calcite component with higher $\frac{1}{[Mg]}$ has lower $\delta^{26}Mg_{cal}$. The upper sample set (XWD-10) collected from ~17 m above XWD-6 (Figure 1b), however, cannot be fitted

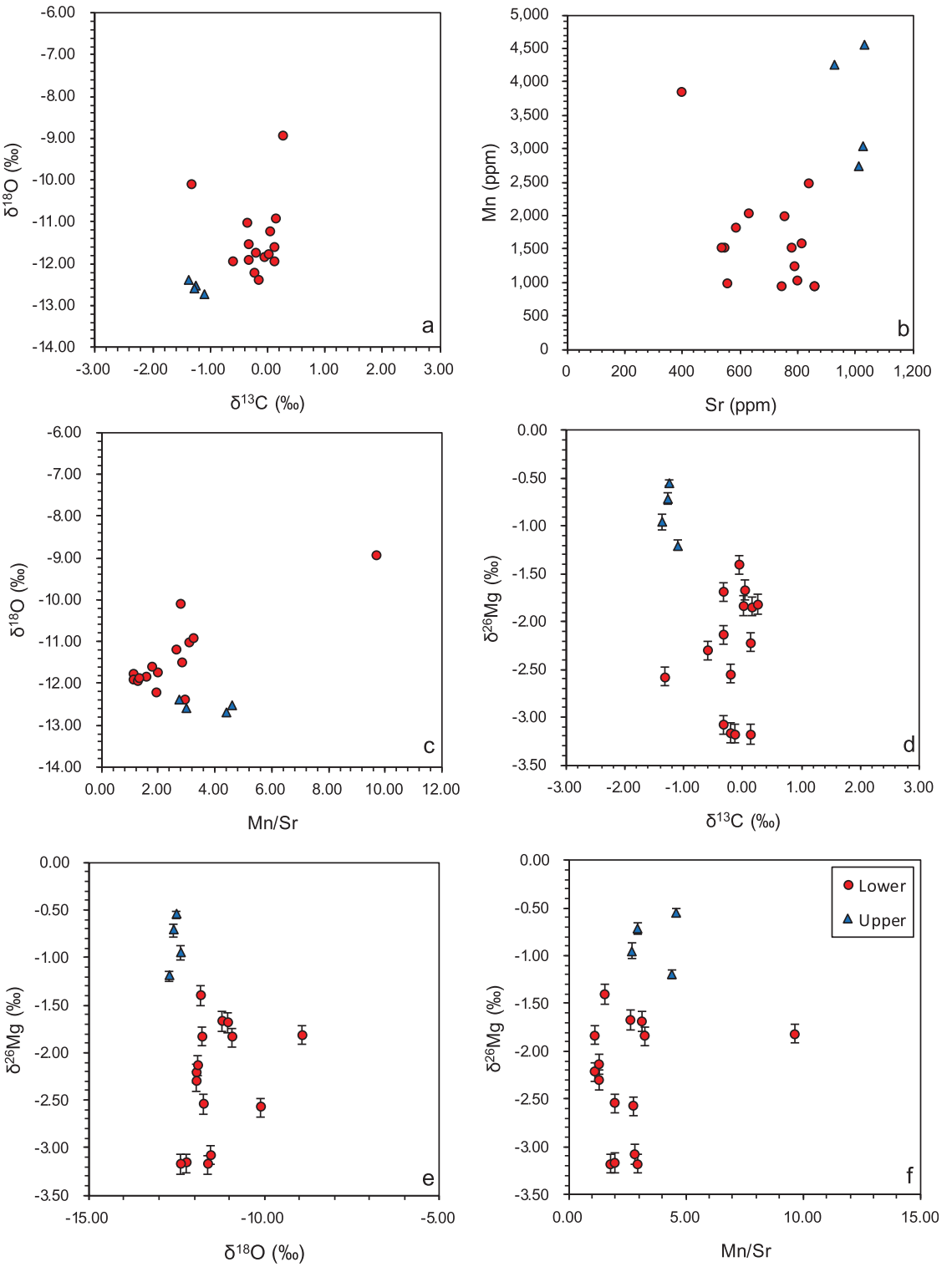

Figure 6. Cross plots of elemental and isotope data of the Xuzhuang limestone. (a) $\delta^{13}C$ versus $\delta^{18}O$. (b) [Sr] versus [Mn]. (c) Mn/Sr versus $\delta^{18}O$. (d) $\delta^{13}C$ versus $\delta^{26}Mg$. (e) $\delta^{18}O$ versus $\delta^{26}Mg$. (f) Mn/Sr versus $\delta^{26}Mg$.

to the regression line defined by the lower sample set (Figures 9a and 9b). This implies that the calcite and dolomite components of upper sample set have different isotopic compositions.

$\delta^{26}Mg_{dol}$ and $\delta^{26}Mg_{cal}$ can be calculated by equations (5) and (6) when both $[Mg]_{cal}$ and $[Mg]_{dol}$ are defined. Alternatively, given unknown $[Mg]_{cal}$, $\delta^{26}Mg_{dol}$ can still be calculated from Figure 9. The slope of ~1 for the

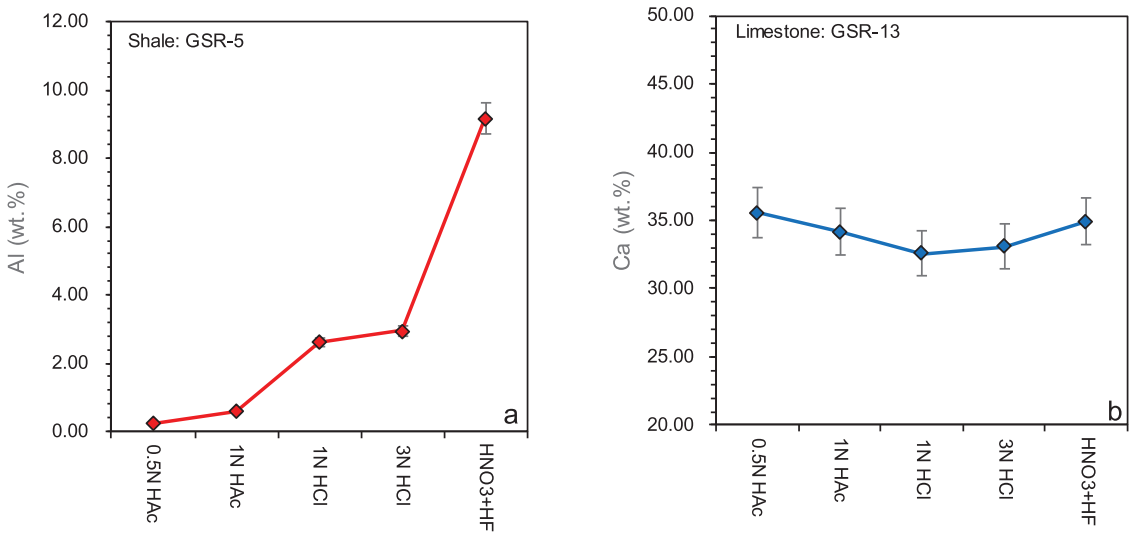

Figure 7. (a) Mg released during shale (GSR-5) dissolution by different types of acids. (b) Ca released during carbonate (GSR-13) dissolution by different types of acids. Samples are completely dissolved by a mixture of concentrated HNO_3 and HF (1:3 in volume ratio). Error bars are 5% uncertainty of ICP-OES analyses.

regression line implies the stoichiometric dolomite [$MgCa(CO_3)_2$ with Mg/Ca = 1] (Figure 8), and $[Mg]_{dol}$ of 0.13 can be used to calculate $\delta^{26}Mg_{dol}$. Thus, the calculated $\delta^{26}Mg_{dol}$ is $-1.6‰$ and $-0.3‰$ for the lower and upper sample sets, respectively. The $\delta^{26}Mg_{dol}$ difference between the lower and upper sample sets cannot be explained by the mineralogical differences (Figure 4). Neither could it be attributed to the post dolomitization diagenetic alterations, because $\delta^{26}Mg$ for dolomite would be preserved during diagenesis, low-grade metamorphism, and dedolomitization [*Azmy et al*., 2013; *Jacobson et al*., 2010; *Li et al*., 2014], and the similar Mn/Sr and $\delta^{18}O$ values for the lower and upper sample sets (Figures 6a and 6b) imply that both sample sets might have undergone the similar degree of diagenetic alteration [*Derry*, 2010; *Kaufman and Knoll*, 1995; *Knauth and Kennedy*, 2009]. Therefore, we suggest that the isotopic difference may record different compositions of the dolomitization fluids and/or the processes of dolomitization. In the following sections, we will demonstrate how to constrain the Mg source and the dolomitization process by Mg isotopes.

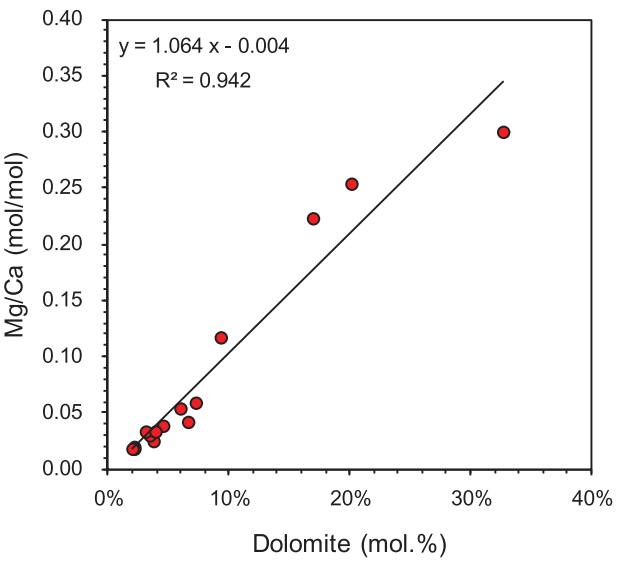

Figure 8. Correlation between Mg/Ca (molar ratio) and dolomite molar fraction in the Xuzhuang limestone samples. Mg/Ca is measured by ICP-OES, while mineralogical compositions are determined by XRD.

6.3. Mg Isotope Systematics of Dolomitization by Advective Flow

In most traditional models, dolomitization occurs when dolomitization fluids percolate through calcareous sediments, and Mg is transported via advective flows [*Machel*, 2004; *Warren*, 2000]. For example, thermal convective flow that is driven by a heat source (Kohout circulation) can cause dolomitization [Aharon *et al*., 1987; *Simms*, 1984]. The reflux model proposes dolomitization by saline brine water generated during evaporation [*Hsü and Siegenthaler*, 1969]. It is also suggested that capillary flow might play an important role in the dolomitization of Sabkha [*Mackenzie et al*., 1980]. Furthermore, mixing model argues for the dolomitization by mixing of seawater and meteoric freshwater [*Ward and Halley*, 1985].

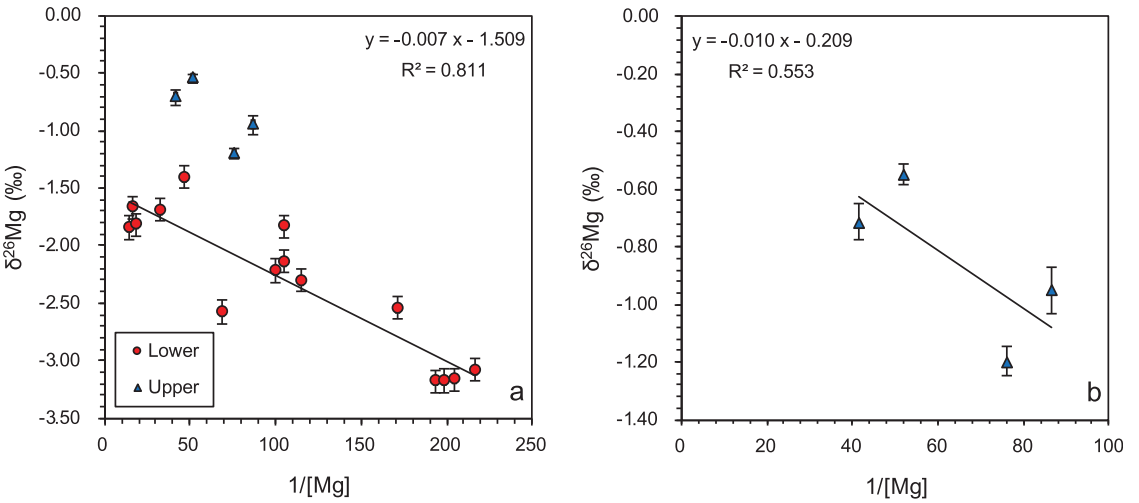

Figure 9. (a) Cross plot showing the negative linear correlation between $\frac{1}{[Mg]}$ and δ^{26}Mg for the lower sample set (XWD-1, XWD-2, XWD-4, XWD-5, and XWD-6) that was collected within a 4 m interval of the lower Xuzhuang Formation. Data for the upper sample set are also shown. (b) Cross plot between $\frac{1}{[Mg]}$ and δ^{26}Mg for the upper sample set (XWD-10, ~17 m above XWD-6 in stratigraphy).

All above dolomitization models involve with advective flow during dolomitization process. Equation for the advective flow (AF) model can be described as following:

$$\frac{\partial[^{i}Mg]}{\partial t} = -v\frac{\partial[^{i}Mg]}{\partial l} - R_i[^{i}Mg] \tag{7}$$

where $[^{i}Mg]$ is the concentration of ^{i}Mg, v is the velocity of advective flow, R_i is the rate constant for Mg removal from porewater, l is the distance from the source of fluids. At steady state ($\frac{\partial[^{i}Mg]}{\partial t}=0$) with invariant v and R_i, equation (7) can be resolved as:

$$[^{i}Mg] = [^{i}Mg]_0 e^{\frac{-R_i l}{v}} \tag{8}$$

As a function of l, $[^{i}Mg]$ remains temporally invariant in a fixed locality (with constant l), but is spatially heterogeneous. The isotopic fractionation during dolomitization is reflected by the difference between the rate constants for ^{24}Mg and ^{26}Mg. The fractionation factor (α_{24}^{26}) is defined by the ratio of rate constants:

$$\frac{R_{26}}{R_{24}} = \alpha_{24}^{26} \tag{9}$$

Mg isotopic composition of dolomitization fluid ($\delta^{26}Mg_{df}$) can be calculated from $[^{24}Mg]$ and $[^{26}Mg]$ by the following equation:

$$\delta^{26}Mg_{df} = [Ln([^{26}Mg/[^{24}Mg]) - Ln([^{26}Mg]_{DSM3}/[^{24}Mg]_{DSM3})] \times 1000 \tag{10}$$

where DSM3 denotes the standard for Mg isotope measurement [*Galy et al*., 2003].

$\delta^{26}Mg_{dol}$ can be calculated as following:

$$\delta^{26}Mg_{dol} = \delta^{26}Mg_{df} - \Delta_{dol} \tag{11}$$

Δ_{dol} is the isotopic fractionation during dolomite formation. Δ_{dol} determined from natural samples varies between 2.0‰ and 2.7‰ [*Fantle and Higgins*, 2014; *Higgins and Schrag*, 2010; *Mavromatis et al*., 2014], which is broadly consistent with the recent experimental results [*Li et al*., 2015]. Based on various experimental studies, the best estimate for Δ_{dol} at surface conditions is ~2.0‰. Thus, $\delta^{26}Mg_{df}$ for the lower and upper sample sets are +0.4‰ and +1.7‰, respectively. Both values are substantially higher than the Mg isotopic composition of modern seawater (−0.8‰) [*Foster et al*., 2010; *Ling et al*., 2011]. There is no constraint on the Mg isotopic composition of Cambrian seawater. It is proposed that Cenozoic seawater has limited variation in δ^{26}Mg based on the study of bulk carbonate samples [*Higgins and Schrag*, 2015], while larger fluctuation

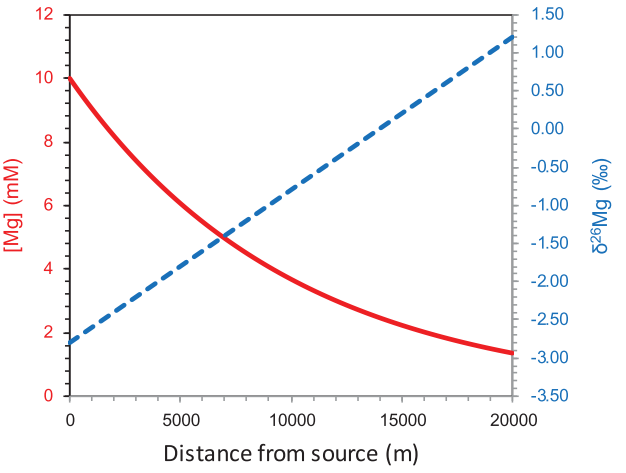

Figure 10. Modeling result of the advective flow model, showing the variation of Mg concentration ([Mg], solid red line, left vertical axis) in the dolomitization fluids and Mg isotopic composition of dolomite ($\delta^{26}Mg_{dol}$, dashed green line, right vertical axis) along the fluid flow pathway. *X* axis indicates the distance from the fluid source. [Mg] decreases, while $\delta^{26}Mg_{dol}$ increases in the flow direction. Assuming normal seawater is the source fluid with $\delta^{26}Mg_0$ of $-0.8‰$, reaction constant for dolomite formation (R) of 0.0001, and the velocity of fluid flow of 100 cm/yr.

of Cenozoic seawater δ^{26}Mg ($0‰\sim-0.8‰$) is obtained from the study of foraminifera tests [*Pogge von Strandmann et al.*, 2014]. In either case, the estimated δ^{26}Mg of Cenozoic seawater is lower than the simulated $\delta^{26}Mg_{df}$, suggesting that dolomitization fluids should be more ^{26}Mg-enriched than seawater, such as compositionally modified seawater or subsurface brine. Because $\delta^{26}Mg_{df}$ increases with distance away from the source region (Figure 10), one possibility is that normal seawater as the primary source of dolomitization fluids, heavy $\delta^{26}Mg_{df}$ may imply that the Xiaweidian area was located in the downstream of the flow (Figure 10).

Furthermore, higher $\delta^{26}Mg_{df}$ of the upper sample set might be interpreted in the following ways: (1) fluid source moving far away from the Xiaweidian area, resulting in the larger distance between the Xiaweidian area and the source region (from 6 to 12.5 km, Figure 11a); (2) an increase in the rate of dolomitization (R = 0.0001–0.00021, Figure 11b); (3) the source fluids more enriched in ^{26}Mg (from $-0.8‰$ to $+0.5‰$, Figure 11c); or (4) a reduction of the velocity of the flow from 100 cm/yr (the assumed default value) to 50 cm/yr (Figure 11d). However, to differentiate these processes, additional analysis is required from multiple sections (see section 6.5).

6.4. Mg Isotope Systematics of Dolomitization by Contemporaneous Seawater

6.4.1. DAR Model Description

In the absence of advective flow, dolomitization may take place via Mg diffusion from the overlying contemporaneous seawater. For example, dolomite formation in the Miocene Monterey Formation is primarily driven by Mg diffusion from the overlying contemporaneous seawater [*Compton and Siever*, 1986]. Such dolomitization process can be modeled by the Diffusion-Advection-Reaction model (DAR) [*Huang et al.*, 2015].

For simplicity, we apply the one-dimensional (1-D) DAR model to quantify $\delta^{26}Mg_{dol}$ of the Xuzhuang limestone. In the 1-D-DAR model, the porewater geochemical profiles are controlled by three physiochemical processes: molecular diffusion, advection, and chemical reaction. The simplified 1D-DAR model can be expressed as:

$$\frac{\partial[^{i}Mg]}{\partial t} = D_{Mg}\frac{\partial^2[^{i}Mg]}{\partial z^2} - s\frac{\partial[^{i}Mg]}{\partial z} - R_i[^{i}Mg] \quad (12)$$

where $[^{i}Mg]$ is porewater concentration of ^{24}Mg or ^{26}Mg, z is depth in sediments, s is sedimentation rate, D_z is diffusivity coefficient, and R_i is the first-order rate constant for ^{24}Mg or ^{26}Mg removal from porewater.

Because there is negligible fractionation in Mg isotope during diffusion ($\alpha^{26/24}_{diffusion} = 1.00006$) [*Richter et al.*, 2006], D_{Mg} is the same for both ^{24}Mg and ^{26}Mg. During dolomitization, replacive dolomite formation is the predominant chemical reaction that consumes porewater Mg^{2+}. Assuming a steady state that porewater profile remains constant through time (i.e., $\frac{\partial[S]}{\partial t} = 0$, and D_{Mg}, R_i ands are constants), equation (12) becomes an ordinary differential equation, and the solution is given by:

$$[^{i}Mg] = [^{i}Mg_0]e^{\frac{[s-(s^2+4R_iD_{Mg})^{\frac{1}{2}}]}{2D_{Mg}}\times z} \quad (13)$$

The porewater Mg isotopic profile ($\delta^{26}Mg_{pw}$) can be calculated by equations (9) and (10). The isotopic composition of instantaneous dolomite formation ($\delta^{26}Mg^{in}_{dol}$) within sediments is determined by $\delta^{26}Mg_{pw}$ and Δ_{dol}:

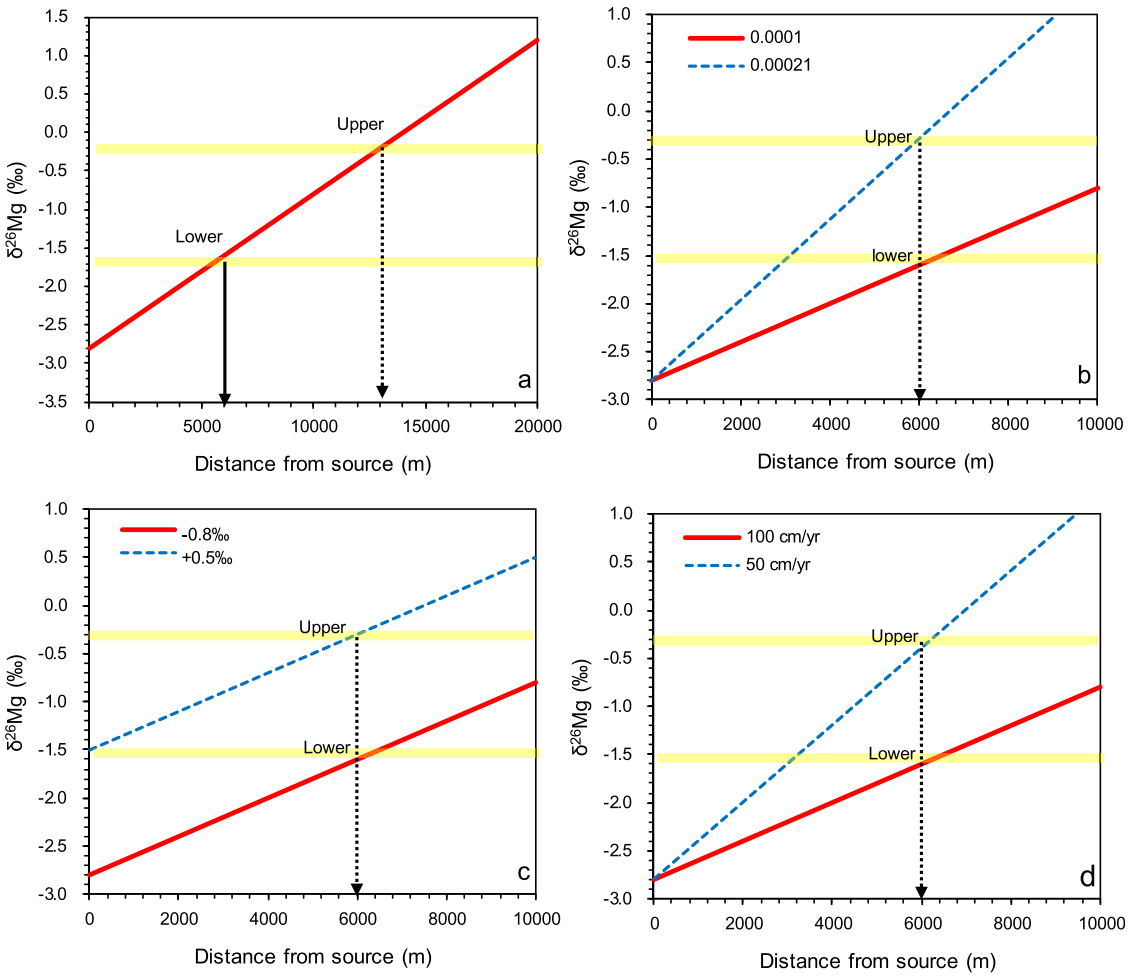

Figure 11. Advective flow modeling results of the lower (solid vertical arrow) and upper (dashed vertical arrow) sample sets of the Xuzhuang limestone. The yellow bands indicate the $\delta^{26}Mg_{dol}$ for the lower (−1.6‰) and upper (−0.3‰) sample sets. (a) Isotopic difference between the lower and upper sample sets is caused by the variation of distance between the Xiaweidian area and the source region of dolomitization fluids. The Xiaweidian section is located at ~6 km downstream from the source region for the lower sample set, and 12.5 km for the upper sample set. (b) Variation in $\delta^{26}Mg_{dol}$ resulted from enhanced reaction rate from 0.0001 (lower sample set) to 0.00021 (upper sample set). (c) Variation in $\delta^{26}Mg_{dol}$ is caused by an increase in $\delta^{26}Mg_0$ from −0.8‰ (lower sample set) to +0.5‰ (upper sample set). (d) Higher $\delta^{26}Mg_{dol}$ of the upper sample set could be the consequence of decrease in the velocity of dolomitization fluid from 100 to 50 cm/yr. The lower sample set is calculated by assuming the source fluid with $\delta^{26}Mg_0$ of −0.8‰, reaction constant for dolomite formation (R) of 0.0001, and the velocity of fluid flow of 100 cm/yr.

$$\delta^{26}Mg_{dol}^{in} = \delta^{26}Mg_{pw} - \Delta_{dol} \tag{14}$$

Because dolomitization is a prolonged process in sediments, and $\delta^{26}Mg_{dol}$ records the cumulative isotope effect throughout the dolomitization process. In order to calculate $\delta^{26}Mg_{dol}$, we divided sediments into multiple slices, each of which has identical thickness of h. The first depth slice represents the place, where dolomitization initiates (i = 1). Within certain depth slice i, the amount of Mg (M^i_{Mg}) being transferred from porewater to dolomite can be calculated by:

$$M^i_{Mg} = [Mg]^i \times R \times \frac{h}{s} \tag{15}$$

The isotopic composition and the content of dolomite can be calculated by the following equations:

$$\delta^{26}Mg_{dol} = \frac{\sum_0^\infty [(\delta^{26}Mg^i_{pw} - \Delta_{dol}) \times M^i_{Mg}]}{\sum_0^\infty M^i_{Mg}} \tag{16}$$

$$M_{dol} = \sum_0^\infty \left([Mg]^i \times R \times \frac{h}{s} \right) \tag{17}$$

To simulate incomplete dolomitization process, it is reasonable to assume that the reaction takes place into infinite depth.

6.4.2. Parameter Setting

In the DAR model, Mg isotopic profiles and Mg isotopic compositions of dolomite are related to the following parameters: D_{Mg}, s, R_{Mg}, $[Mg]_0$, Δ_{dol}, and $\delta^{26}Mg_0$. Diffusion coefficient is temperature dependent, and varies from 3.26×10^{-10} to 6.55×10^{-10} m^2s^{-1} in seawater and 1.6×10^{-10} to 3.3×10^{-10} m^2s^{-1} within sediment with 60% porosity (D_{Mg}) at temperatures between 0°C and 25°C. We choose 2.5×10^{-10} as the default value in simulation. The depositional rate (s) for normal marine non-reef carbonate ranges from 1 to 10 cm/ky [*Tucker and Wright*, 1990]. The intermediate value of 5 cm/ky is used in this study.

Because dolomitization can initiate at any sediment depth below the water-sediment interface (WSI) and $[Mg]_{pw}$ decreases through sediment depth [*Higgins and Schrag*, 2010], $[Mg]_0$ should be no larger than the Cambrian seawater value of 100 m*M* [*Hardie*, 1996]. For simplicity, we assume that dolomitization begins near WSI with $[Mg]_0$ of 100 m*M*. The absolute value of the rate constant for dolomitization is unconstrained. Accordingly, we keep R_{Mg} tunable in our model. The optimum value for the fractionation for dolomite precipitation (Δ_{dol}) is 2.0‰ as mentioned earlier.

6.4.3. Modeling Results

By assigning the aforementioned parameters with the default values ($D_{Mg} = 2.5 \times 10^{-10}$ m^2s^{-1}, s = 5 cm/ky, $[Mg]_0 = 100$m*M*, and $\Delta_{dol} = 2.0‰$), R_{Mg} and $\delta^{26}Mg_0$ can be uniquely resolved. In order to generate 4 wt % of dolomite (assuming rock density of 2.5g/cm^3), ~0.5 mol Mg is required for every 1 L of rocks (i.e., ~0.36 mol Mg from every liter of pore fluids in sediments with 60% porosity).To simulate both the dolomite content (4 wt %) and $\delta^{26}Mg_0$ (−1.6‰) of the lower sample set, R_{Mg} and $\delta^{26}Mg_0$ are 0.000003 and −0.75‰, respectively. For the upper sample set with ~4 wt.% dolomite and $\delta^{26}Mg_{dol}$ of −0.3‰, the simulated R_{Mg} and $\delta^{26}Mg_0$ are 0.000003 and +0.55‰, respectively (Figures 12c and 12d). The DAR model also shows that, in case of the lower sample set, $\delta^{26}Mg_{dol}$ increases with depth, and becomes invariant at ~300 m below the WSI, about 6 million years after limestone deposition (Figure 12a). Below this depth, $\delta^{26}Mg_{dol}$ show limited variation, and is stabilized at −1.59‰ with dolomite content accounting for ~4 wt.% of total mass (Figure 12b).

6.4.4. Sensitivity Test

In order to test the sensitivity of the modeling parameters, we initiate with the default values and sequentially modify each single parameter. Both dolomite content and $\delta^{26}Mg_{dol}$ are simulated in each run.

To test the sensitivity to D_{Mg}, D_{Mg} is allowed to vary from 1.6×10^{-10} to 3.3×10^{-10} m^2s^{-1}, corresponding to the reaction temperatures ranging from 0°C to 25°C. There is only 0.05‰ variation in $\delta^{26}Mg_{dol}$, and dolomite content varies between 3.3% and 4.6% (Figure 13a), suggesting that $\delta^{26}Mg_{dol}$ is not sensitive to D_{Mg} at room temperature. The sedimentation rate is allowed to vary from 0.2 to 20 cm/ky. With an increase in the sedimentation rate, there is a sharp decrease of the dolomite content from 85% to 1.6%, and a 0.5‰ increase in $\delta^{26}Mg_{dol}$ from −1.75‰ to −1.21‰ (Figure 13b). Thus, dolomite production rate is significantly affected by sedimentation rate, while $\delta^{26}Mg_{dol}$ is moderately affected. The seawater [Mg] is the maximum bound for $[Mg]_0$. $\delta^{26}Mg_{dol}$ is independent of this parameter, but dolomite content decreases from 4% to 0.2% when $[Mg]_0$ decreases from 100 m*M* to 5 m*M* (Figure 13c). For R_{Mg} that is completely unconstrained in the modeling, we run a sensitivity test with four orders of magnitude of variation (from 0.003 to 0.0000003). With the decreasing of R_{Mg} from 0.003 to 0.0000003, $\delta^{26}Mg_{dol}$ is moderately affected (increasing from −1.89‰ to −1.44‰), but the dolomite content experiences a sharp decline from 92% to 1.7% (Figure 13d). Increasing Δ_{dol} from 1.5‰ to 2.7‰, $\delta^{26}Mg_{dol}$ shows a reverse trend with smaller range of variation, decreasing from −1.38‰ to −1.89‰ (Figure 13e). Finally, a 2.5‰ variation is allowed for $\delta^{26}Mg_0$ (ranging from −1.5‰ to +1.0‰). Dolomite content remains invariant, but $\delta^{26}Mg_{dol}$ shows a similar trend of variation with the same magnitude (−2.34‰ to 0.16‰) (Figure 13f).

Therefore, for the contemporaneous seawater dolomitization, dolomite content is particularly sensitive to s, R_{Mg}, and $[Mg]_0$, independent of Δ_{dol} and $\delta^{26}Mg_0$, and moderately affected by D_{Mg}. In contrast, $\delta^{26}Mg_{dol}$ is not affected by $[Mg]_0$, insensitive to D_{Mg}, moderately sensitive to s and R_{Mg}, but sensitive to Δ_{dol} and $\delta^{26}Mg_0$. Because Δ_{dol} is only slightly affected by temperature (−2.1‰ to −1.8‰ from 0°C and 25°C) [*Li et al*, 2015], $\delta^{26}Mg_{dol}$ is mainly affected by $\delta^{26}Mg_0$, which is a function of initial sediment depth for dolomitization. Thus, $\delta^{26}Mg_{dol}$ might be used to constrain the initiation depth or the timing of dolomitization.

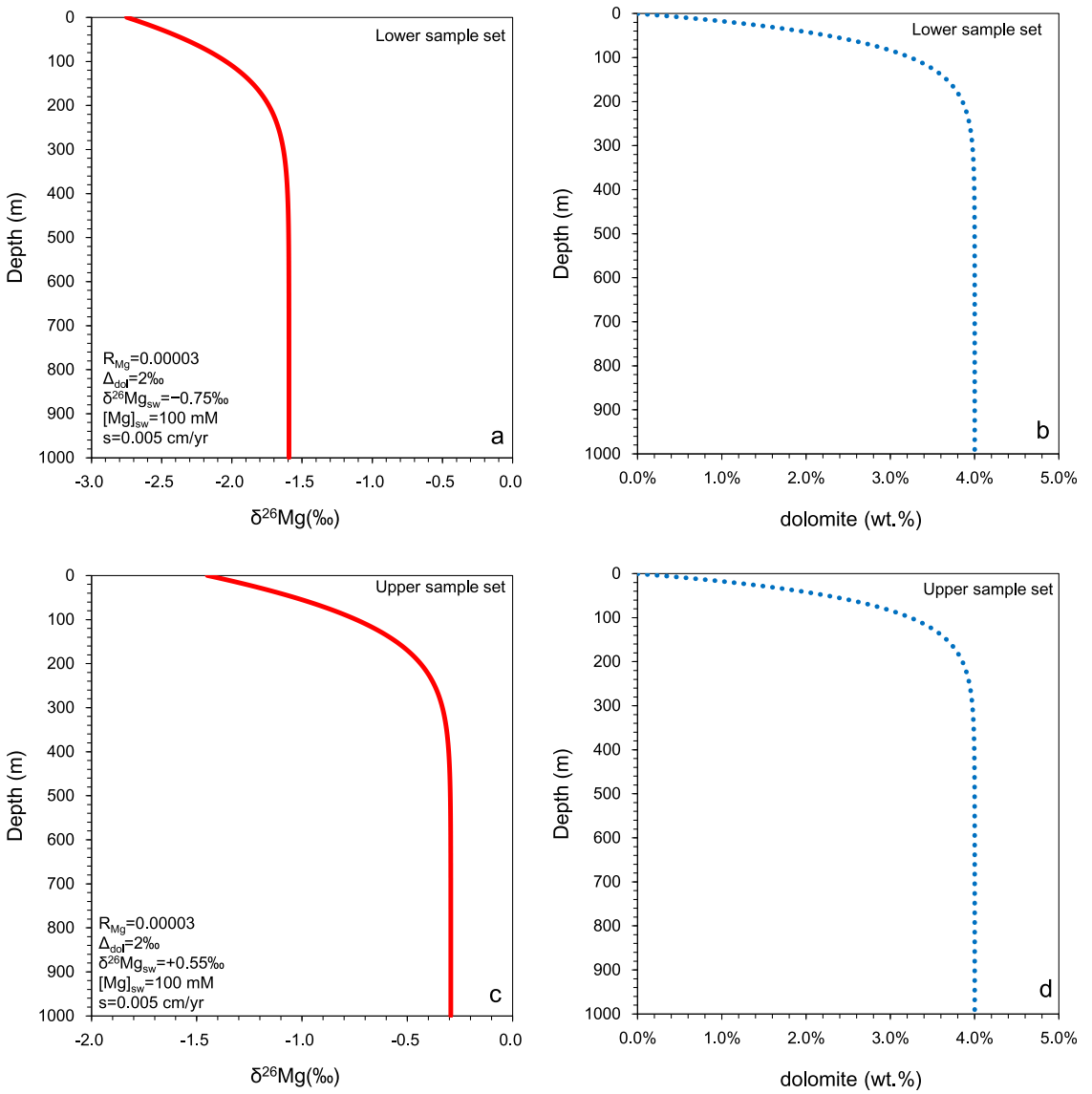

Figure 12. Modeling results of the 1D-DAR model with the default boundary conditions (section 6.4.2), and assuming contemporaneous seawater dolomitization begins at the WSI. (a) $\delta^{26}Mg_{dol}$ profile of the lower sample set. (b) Depth profile of dolomite content of the lower sample set. (c) $\delta^{26}Mg_{dol}$ profile of the upper sample set. (d) Depth profile of dolomite content of the upper sample set.

6.5. Using Mg Isotope to Constrain Dolomite Formation

Mg isotopic composition of the dolomite component in the Xuzhuang limestone can be simulated by both AF and DAR models, although these two models describe fundamentally different dolomitization processes. In the AF model, given known Δ_{dol}, isotopic composition of dolomitization fluids ($\delta^{26}Mg_{df}$) can be uniquely determined by $\delta^{26}Mg_{dol}$. In the DAR model, although Mg isotopic systematics of dolomitization would be affected by multiple parameters, $\delta^{26}Mg_{dol}$ is most sensitive to the isotopic composition of initial dolomitization fluids ($\delta^{26}Mg_0$, representing isotopic composition of contemporaneous seawater or porewater at depth of initial dolomitization). It is widely accepted that various types of fluids could provide Mg for dolomitization, including contemporaneous seawater, modified seawater, brine water, mixing between seawater and freshwater, and various subsurface fluids [*Machel*, 2004; *Warren*, 2000], and these dolomitization fluids have a wide-range of Mg isotopic compositions [*de Villiers et al.*, 2005; *Foster et al.*, 2010; *Higgins and Schrag*, 2010; *Ling et al.*, 2011; *Pogge von Strandmann et al.*, 2008; *Tipper et al.*, 2008, 2010]. Therefore, Mg isotopes can be used to constrain the source of dolomitization fluids.

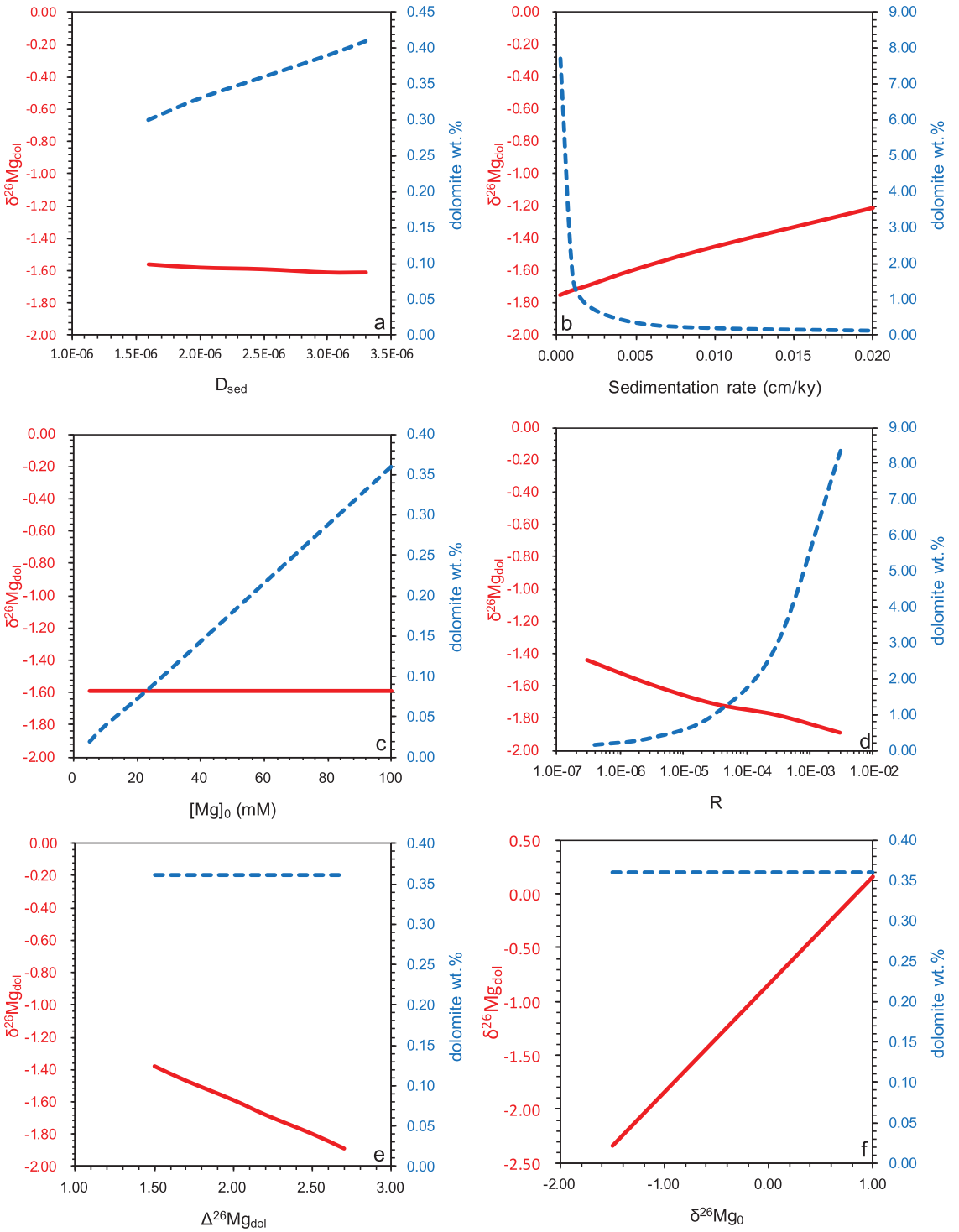

Figure 13. Sensitivity tests of the DAR model. Both $\delta^{26}Mg_{dol}$ (red solid line, left vertical axis) and dolomite wt. % (blue-dashed line, right vertical axis) are tested by adjusting a single parameter. (a) Diffusion coefficient (D_{Mg}). (b) Sedimentation rate (s). (c) Seawater Mg concentration ($[Mg]_0$). (d) Reaction rate constant (R). (e) Isotopic fractionation for dolomite formation (Δ_{dol}). (f) Mg isotopic composition of seawater ($\delta^{26}Mg_0$).

As shown in this exercise, the modeling results from the AF and DAR models are different, suggesting that Mg isotope systematics of dolomitization is complex. The simulated $\delta^{26}Mg_{df}$ in the AF model is significantly heavier than the seawater value (Figure 10), suggesting that the dolomitization fluid might have derived

from certain ^{26}Mg-enriched fluids, such as brine fluids, fluids with clay-derived Mg, or dolomitization occurs in the downstream of advective flow (Figure 11). In the DAR model, the lower sample set of the Xuzhuang limestone can be simulated by the contemporaneous seawater dolomitization initiating at WSI, while the dolomitization of the upper sample set might start within sediments after burial (Figure 12).

In order to further differentiate these two dolomitization processes, samples from multiple localities are required. The AF model predicts spatially heterogeneous $\delta^{26}Mg_{dol}$, which is characterized by the downstream enrichment of ^{26}Mg (Figure 10). On the contrary, contemporaneous seawater dolomitization theoretically generates dolomites with spatially homogeneous $\delta^{26}Mg_{dol}$.

Therefore, using Mg isotope to constrain dolomitization is theoretically plausible, but may not be straightforward in application. We argue that it is difficult to constrain the dolomitization process by Mg isotopes just based on the study of a single section; instead correlatable carbonate samples from multiple sections are required. Particularly, sampling under the guidance of high-resolution bio-, chemo-, and chronostratigraphic frameworks would dramatically benefit this type of research.

7. Conclusions

Partially dolomitized limestones from the middle Cambrian Xuzhuang Formation have a wide range of variation in δ^{26}Mg ($-0.55‰ \sim -3.18‰$). There is a negative linear correlation between δ^{26}Mg and $\frac{1}{[Mg]}$, suggesting a binary mixing between the calcite and dolomite components. Mg isotopic composition of the dolomite component ($\delta^{26}Mg_{dol}$) of the lower sample set is $-1.6‰$, significantly lower than that of the upper sample set with $\delta^{26}Mg_{dol}$ of $-0.3‰$. However, either mineralogical compositions, C and O isotopes, or petrographic features cannot be used as the diagnostic criteria to differentiate dolomite in these two batches of samples. To quantify the Mg isotope systematics during dolomitization, we apply the Advective Flow (AF) model and the Diffusion-Advection-Reaction (DAR) model. In the AF model, advective fluid flow is responsible for Mg transport, whereas Mg is transferred by diffusion in the DAR model. The AF model can applied to most traditional hydrodynamic dolomitization models, while the DAR model simulates dolomitization by contemporaneous seawater. The AF modeling result indicates that δ^{26}Mg of dolomitization fluid are $+0.4‰$ and $+1.7‰$ for the lower and upper sample sets (assuming $\Delta_{dol}=2.0‰$), excluding normal seawater could as the direct Mg source. In contrast, both dolomite content and $\delta^{26}Mg_{dol}$ of the lower sample set can be simulated by the DAR model by using seawater δ^{26}Mg value of $-0.75‰$, while much heavier seawater δ^{26}Mg of $+0.7‰$ is required to simulate the upper sample set. The AF model predicts a spatially heterogeneous $\delta^{26}Mg_{dol}$ showing an increasing trend along the flow pathway, in contrast, the DAR model predicts a spatially homogeneous $\delta^{26}Mg_{dol}$. Thus, dolomitization process can be constrained by Mg isotopes, if multiple sections are studied.

Acknowledgments

The data for this paper are available by contacting with Bing Shen. Email: bingshen@pku.edu.cn. This study is supported by Natural Science Foundation of China (41272017 and 41322021). We thank Linda Kah and an anonymous reviewer for constructive comments on the earlier versions of the manuscript, and Chuanming Zhou (Nanjing Institute of Geology and Paleontology, CAS) for C and O isotope analyses.

References

Aharon, P., R. A. Socki, and L. Chan (1987), Dolomitization of Atolls by sea water convection flow: Test of a hypothesis at Niue, South Pacific, *J. Geol.*, *95*(2), 187–203.

Awwiller, D. N. (1993), Illite/smectite formation and potassium mass transfer during burial diagenesis of mudrocks: A study from the Texas Gulf Coast Paleocene-Eocene, *J. Sediment. Res.*, *63*(3), 501–512.

Azmy, K., D. Lavoie, Z. Wang, U. Brand, I. Al-Aasm, S. Jackson, and I. Girard (2013), Magnesium-isotope and REE compositions of Lower Ordovician carbonates from eastern Laurentia: Implications for the origin of dolomites and limestones, *Chem. Geol.*, *356*, 64–75.

Badiozam, K. (1973), Dorag dolomitization model-Application to middle Ordovician of Wisconsin, *J. Sediment. Petrol.*, *43*(4), 965–984.

Chen, J. (2009), Limestone pseudoconglomerates in the Late Cambrian Gushan and Chaomidian Formations (Shandong Province, China): Soft-sediment deformation induced by storm-wave loading, *Sedimentology*, *56*, 1174–1195.

Chen, J., Z. Han, X. Zhang, A. Fan, and R. Yang (2010), Early diagenetic deformation structures of the Furongian ribbon rocks in Shandong Province of China: A new perspective of the genesis of limestone conglomerates, *Sci. China Earth Sci.*, *53*(2), 241–252.

Compton, J. S., and R. Siever (1986), Diffusion and mass balance of Mg during early dolomite formation, Monterey Formation, *Geochim. Cosmochim. Acta*, *50*(1), 125–135.

de Villiers, S., J. A. D. Dickson, and R. M. Ellam (2005), The composition of the continental river weathering flux deduced from seawater Mg isotopes, *Chem. Geol.*, *216*(1-2), 133–142.

Derry, L. A. (2010), On the significance of δ^{13}C correlations in ancient sediments, *Earth Planet. Sci. Lett.*, *296*(3-4), 497–501.

Fantle, M. S., and J. Higgins (2014), The effects of diagenesis and dolomitization on Ca and Mg isotopes in marine platform carbonates: Implications for the geochemical cycles of Ca and Mg, *Geochim. Cosmochim. Acta*, *142*(0), 458–481.

Feng, Z., Y. Peng, Z. Jin, and Z. Bao (2002), Lithofacies palaeogeography of the Middle Cambrian in China, *J. Palaeogeogr.*, *4*(2), 1–11.

Foster, G. L., P. A. E. Pogge von Strandmann, and J. W. B. Rae (2010), Boron and magnesium isotopic composition of seawater, *Geochem. Geophys. Geosyst.*, *11*, Q08015, doi:10.1029/2010GC003201.

Galy, A., et al. (2003), Magnesium isotope heterogeneity of the isotopic standard SRM980 and new reference materials for magnesium-isotope-ratio measurements, *J. Anal. At. Spectrom.*, *18*, 1352–1356.
Gao, L., and X. Qiao (2001), Cambrian Xiaweidian Formation, a newly established formation in Western Hills, Beijing, *J. Stratigr.*, *25*, 188–192.
Gao, L., C. Zhang, P. Liu, F. Tang, B. Song, and X. Ding (2009), Reclassification of the Meso- and Neoproterozoic chronostratigraphy of North China by SHRIMP zircon ages, *Acta Geol. Sin.*, *83*, 1074–1084.
Geske, A., S. Lokier, M. Dietzel, D. K. Richter, D. Buhl, and A. Immenhauser (2015a), Magnesium isotope composition of sabkha porewater and related (Sub-)Recent stoichiometric dolomites, Abu Dhabi (UAE), *Chem. Geol.*, *393–394*, 112–124.
Geske, A., R. H. Goldstein, V. Mavromatis, D. K. Richter, D. Buhl, T. Kluge, C. M. John, and A. Immenhauser (2015b), The magnesium isotope (δ26Mg) signature of dolomites, *Geochim. Cosmochim. Acta*, *149*, 131–151.
Goldsmith, J. R. (1953), A "Simplexity Principle" and Its Relation to "Ease" of Crystallization, *J. Geol.*, *61*(5), 439–451.
Hardie, L. A. (1996), Secular variation in seawater chemistry: An explanation for the coupled secular variation in the mineralogies of marine limestones and potash evaporites over the past 600 my, *Geology*, *24*(3), 279–283.
Higgins, J. A., and D. P. Schrag (2010), Constraining magnesium cycling in marine sediments using magnesium isotopes, *Geochim. Cosmochim. Acta*, *74*(17), 5039–5053.
Higgins, J. A., and D. P. Schrag (2015), The Mg isotopic composition of Cenozoic seawater – evidence for a link between Mg-clays, seawater Mg/Ca, and climate, *Earth Planet. Sci. Lett.*, *416*, 73–81.
Hsü, K. J., and C. Siegenthaler (1969), Preliminary experiments on hydrodynamic movement induced by evaporation and their bearing on the dolomite problem, *Sedimentology*, *12*(1-2), 11–25.
Huang, K.-J., B. Shen, X.-G. Lang, W.-B. Tang, Y. Peng, S. Ke, A. J. Kaufman, H.-R. Ma, and F.-B. Li (2015), Magnesium isotopic compositions of the Mesoproterozoic dolostones: Implications for Mg isotopic systematics of marine carbonate, *Geochim. Cosmochim. Acta*, *164*, 333–351.
Jacobson, A. D., Z. Zhang, C. Lundstrom, and F. Huang (2010), Behavior of Mg isotopes during dedolomitization in the Madison Aquifer, South Dakota, *Earth Planet. Sci. Lett.*, *297*(3-4), 446–452.
Kahle, C. F. (1965), Possible roles of clay minerals in the formation of dolomite, *J. Sediment. Res.*, *35*, 448–453.
Kaufman, A. J., and A. H. Knoll (1995), Neoproterozoic variations in the C-isotope composition of sea water: Stratigraphic and biogeochemical implications, *Precambrian Res.*, *73*(3-4), 27–49.
Knauth, L. P., and M. J. Kennedy (2009), The late Precambrian greening of the Earth, *Nature*, *460*(7256), 728–732.
Land, L. S. (1985), The origin of massive dolomite, *J. Geol.l Educ.*, *33*, 112–125.
Land, L. S. (1998), Failure to precipitate dolomite at 25 degrees C from dilute solution despite 1000-fold oversaturation after 32 years, *Aquat. Geochem.*, *4*(3-4), 361–368.
Li, W.-Y., F.-Z. Teng, B. A. Wing, and Y. Xiao (2014), Limited magnesium isotope fractionation during metamorphic dehydration in metapelites from the Onawa contact aureole, Maine, *Geochem. Geophys. Geosyst.*, *15*, 408–415, doi:10.1002/2013GC004992.
Li, W., B. L. Beard, C. Li, H. Xu, and C. M. Johnson (2015), Experimental calibration of Mg isotope fractionation between dolomite and aqueous solution and its geological implications, *Geochim. Cosmochim. Acta*, *157*, 164–181.
Ling, M.-X., F. Sedaghatpour, F.-Z. Teng, P. D. Hays, J. Strauss, and W. Sun (2011), Homogenous magnesium isotopic composition of seawater, *Rapid Commun. Mass Spectrom.*, *25*, 2828–2836.
Machel, H.-G. (1985), Cathodoluminescence in Calcite and Dolomite and Its Chemical Interpretation, *Geoscience Canada*, *12*, 139–147.
Machel, H. G. (2004), Concepts and models of dolomitization: A critical reappraisal, *Geol. Soc. Spec. Publ.*, *235*(1), 7–63.
Machel, H.-G., and E. W. Mountjoy (1986), Chemistry and environments of dolomitization: A reappraisal, *Earth Sci. Rev.*, *23*(3), 175–222.
Machel, H. G., R. A. Mason, A. N. Mariano, and A. Mucci (1991), Cause and emission of luminescence in calcite and dolomite, in *Luminescence Microscopy: Quantitative and Qualitative Aspects*, edited by C. E. Barker and O. C. Kopp, pp. 16–33, Soc. of Sediment. Geol., Dallas, Tex.
Mackenzie, J., K. J. Hsu, and J. F. Schneider (1980), Movement of subsurface waters under the sabkha, Abu Dhabi, UAE and its relation to evaporative dolomite genesis, *SEPM Spec. Publ.*, *28*, 11–30.
Mavromatis, V., P. Meister, and E. H. Oelkers (2014), Using stable Mg isotopes to distinguish dolomite formation mechanisms: A case study from the Peru Margin, *Chem. Geol.*, *385*, 84–91.
Mazzullo, S. J. (2000), Organogenic dolomitization in peritidal to deep-sea sediments, *J. Sediment. Res.*, *70*(1), 10–23.
Mei, M., Y. Ma, J. Deng, and H. Chen (2005), From cycles to sequences: Sequence stratigraphy and relative sea level change for the Late Cambrian of the North China Platform., *Acta Geol. Sin.*, *79*, 372–383.
Munnecke, A., and C. Samtleben (1996), The formation of micritic limestones and the development of limestone-marl alternations in the Silurian of Gotland, Sweden, *Facies*, *34*(1), 159–176.
Opfergelt, S., R. B. Georg, B. Delvaux, Y. M. Cabidoche, K. W. Burton, and A. N. Halliday (2012), Mechanisms of magnesium isotope fractionation in volcanic soil weathering sequences, Guadeloupe, *Earth Planet. Sci. Lett.*, *341–344*, 176–185.
Osleger, D., and J. F. Read (1991), Relation of eustasy to stacking patterns of meter-scale carbonate cycles, Late Cambrian, U.S.A, *J. Sediment. Res.*, *61*(7), 1225–1252.
Pogge von Strandmann, P. A. E., K. W. Burton, R. H. James, P. van Calsteren, S. R. Gislason, and B. Sigfússon (2008), The influence of weathering processes on riverine magnesium isotopes in a basaltic terrain, *Earth Planet. Sci. Lett.*, *276*(1-2), 187–197.
Pogge von Strandmann, P. A. E., T. Elliott, H. R. Marschall, C. Coath, Y.-J. Lai, A. B. Jeffcoate, and D. A. Ionov (2011), Variations of Li and Mg isotope ratios in bulk chondrites and mantle xenoliths, *Geochim. Cosmochim. Acta*, *75*, 5247–5268.
Pogge von Strandmann, P. A. E., J. Forshaw, and D. N. Schmidt (2014), Modern and Cenozoic records of seawater magnesium from foraminiferal Mg isotopes, *Biogeosciences*, *11*, 5155–5168.
Richter, F. M., R. A. Mendybaev, J. N. Christensen, I. D. Hutcheon, R. W. Williams, N. C. Sturchio, and A. D. Beloso Jr (2006), Kinetic isotopic fractionation during diffusion of ionic species in water, *Geochim. Cosmochim. Acta*, *70*(2), 277–289.
Roberts, J. A., P. A. Kenward, D. A. Fowle, R. H. Goldstein, L. A. González, and D. S. Moore (2013), Surface chemistry allows for abiotic precipitation of dolomite at low temperature, *Proc. Natl. Acad. Sci. U. S. A.*, *110*, 14,540–14,545.
Rosen, M. R., D. E. Miser, and J. K. Warren (1988), Sedimentology, mineralogy and isotopic analysis of Pellet Lake, Coorong region, South Australia, *Sedimentology*, *35*(1), 105–122.
Rustad, J. R., W. H. Casey, Q. Z. Yin, E. J. Bylaska, A. R. Felmy, S. A. Bogatko, V. E. Jackson, and D. A. Dixon (2010), Isotopic fractionation of Mg^{2+}(aq), Ca^{2+}(aq), and Fe^{2+}(aq) with carbonate minerals, *Geochim. Cosmochim. Acta*, *74*(22), 6301–6323.
Schauble, E. A. (2011), First-principles estimates of equilibrium magnesium isotope fractionation in silicate, oxide, carbonate and hexaaquamagnesium(2+) crystals, *Geochim. Cosmochim. Acta*, *75*(3), 844–869.

Shen, B., B. Jacobsen, C.-T. A. Lee, Q.-Z. Yin, and D. M. Morton (2009), The Mg isotopic systematics of granitoids in continental arcs and implications for the role of chemical weathering in crust formation, *Proc. Natl. Acad. Sci. U. S. A.*, *106*, 20,652–20,657

Shen, B., J. Wimpenny, C.-T. A. Lee, D. Tollstrup, and Q.-Z. Yin (2013), Magnesium isotope systematics of endoskarns: Implications for wall-rock reaction in magma chambers, *Chem. Geol.*, *356*, 209–214.

Simms, M. (1984), Dolomitization by groundwater-flow system in carbonate platforms, *Gulf Coast Assoc. Geol. Soc. Trans.*, *34*, 411–420.

Tipper, E. T., A. Galy, and M. J. Bickle (2006a), Riverine evidence for a fractionated reservoir of Ca and Mg on the continents: Implications for the oceanic Ca cycle, *Earth Planet. Sci. Lett.*, *247*(3-4), 267–279.

Tipper, E. T., A. Galy, J. Gaillardet, M. J. Bickle, H. Elderfield, and E. A. Carder (2006b), The magnesium isotope budget of the modern ocean: Constraints from riverine magnesium isotope ratios, *Earth Planet. Sci. Lett.*, *250*, 241–253.

Tipper, E. T., A. Galy, and M. J. Bickle (2008), Calcium and magnesium isotope systematics in rivers draining the Himalaya-Tibetan-Plateau region: Lithological or fractionation control?, *Geochim. Cosmochim. Acta*, *72*(4), 1057–1075.

Tipper, E. T., J. Gaillardet, P. Louvat, F. Capmas, and A. F. White (2010), Mg isotope constraints on soil pore-fluid chemistry: Evidence from Santa Cruz, California, *Geochim. Cosmochim. Acta*, *74*(14), 3883–3896.

Tucker, M. E., and V. P. Wright (1990), *Carbonate Sedimentology*, 482 pp., Blackwell Sci., Oxford.

Vasconcelos, C., and J. A. McKenzie (1997), Microbial mediation of modern dolomite precipitation and diagenesis under anoxic conditions (Lagoa Vermelha, Rio de Janeiro, Brazil), *J. Sediment. Res.*, *67*(3), 378–390.

Vasconcelos, C., J. A. McKenzie, S. Bernasconi, D. Grujic, and A. J. Tiens (1995), Microbial mediation as a possible mechanism for natural dolomite formation at low temperatures, *Nature*, *377*(6546), 220–222.

Wang, H. (1985), *Atlas of the Palaeogeography of China*, 143 pp., Cartogr. Publ. House, Beijing.

Wanless, H. R. (1982), Limestone response to stress; Pressure solution and dolomitization; reply, *J. Sediment. Res.*, *52*(1), 328–332.

Ward, W. C., and R. B. Halley (1985), Dolomitization in a mixing zone of near-seawater composition, Late Pleistocene, northeastern Yucatan Peninsula, *J. Sediment. Res.*, *55*, 407–420.

Warren, J. (2000), Dolomite: Occurrence, evolution and economically important associations, *Earth Sci. Rev.*, *52*(1-3), 1–81.

Westphal, H., and A. Munnecke (2003), Limestone-marl alternations: A warm-water phenomenon?, *Geology*, *31*(3), 263–266.

Westphal, H., M. J. Head, and A. Munnecke (2000), Differential diagenesis of rhythmic limestone alternations supported by palynological evidence, *J. Sediment. Res.*, *70*(3), 715–725.

Wimpenny, J., C. A. Colla, Q.-Z. Yin, J. R. Rustad, and W. H. Casey (2014), Investigating the behaviour of Mg isotopes during the formation of clay minerals, *Geochim. Cosmochim. Acta*, *128*, 178–194.

Zhang, F., H. Xu, H. Konishi, J. M. Kemp, E. E. Roden, and Z. Shen (2012), Dissolved sulfide-catalyzed precipitation of disordered dolomite: Implications for the formation mechanism of sedimentary dolomite, *Geochim. Cosmochim. Acta*, *97*, 148–165.

Zhu, Y., and L. Ma (2008), Division and correlation of Lower Cambrian and its sedimentary evolution in North China, *Geol. Rev. 54*, 731–740.